2024-05-01

Comparative Analysis Of The Effects Of Post Processing On The Flexural Fatigue Endurance Of Additively Manufactured Ti-6Al-4V

Cristian Banuelos
University of Texas at El Paso

COMPARATIVE ANALYSIS OF THE EFFECTS OF POST PROCESSING ON THE FLEXURAL FATIGUE ENDURANCE OF ADDITIVELY MANUFACTURED TI-6AL-4V

CRISTIAN BANUELOS

Master's Program in Mechanical Engineering

APPROVED:

Francisco Medina, Ph.D., Chair

Edel Arrieta, Ph.D.

Ryan Wicker, Ph.D.

Amit Lopes, Ph.D.

Stephen L. Crites, Jr., Ph.D.
Dean of the Graduate School

Dedication

I dedicate this thesis to my parents, whose unwavering love, support, and encouragement have been fundamental throughout my educational journey. They have inspired me and given me the strength to persevere.

COMPARATIVE ANALYSIS OF THE EFFECTS OF POST PROCESSING ON THE FLEXURAL FATIGUE ENDURANCE OF ADDITIVELY MANUFACTURED TI-6AL-4V

by

CRISTIAN BANUELOS, B.S.

THESIS

Presented to the Faculty of the Graduate School of

The University of Texas at El Paso

in Partial Fulfillment

of the Requirements

for the Degree of

MASTER OF SCIENCE

Department of Aerospace and Mechanical Engineering
THE UNIVERSITY OF TEXAS AT EL PASO
May 2024

Acknowledgements

I would like to express my deepest gratitude to my research advisor, Dr. Francisco Medina and mentor Dr. Edel Arrieta for their invaluable guidance, mentorship, and unwavering support throughout my academic career at Keck Center. Thank you for pushing me to pursue avenues I had never imagined for myself.

I would also like to thank my fellow lab mates and the new friendships I made during the course of my studies. Collaborating with all of you has been quite a journey and I hope the best for all of you, wherever your paths may take you.

Lastly, I would like to thank my parents for their sacrifices that allowed me to be the person that I am today. My strife for greatness is only to honor all the things you have done for me and my brother. Thank you again and I hope to keep making you proud.

Abstract

This study delves into analyzing the effects of various machining techniques on the flexural fatigue life of Ti-6Al-4V L-PBF specimens. The fatigue life and fracture behavior of specimens subjected to milling, grinding, polishing, and abrasive media blasting were compared. The findings reveal significant differences in the fatigue resistance between machined and non-machined parts. This study contributes to the understanding of the effects of post-processing on the durability of L-PBF manufactured components, offering insights for enhancing their application in critical aerospace and biomedical applications.

Table of Contents

List of Tables

List of Figures

Chapter 1: Literature Review

1.1 Additive Manufacturing

Additive manufacturing (AM), often referred to as 3D printing, is a manufacturing method in which the part(s) or specimen(s) are produced in a layer based manner [1]. This contrasts with more traditional techniques, with regards to the production of metal components, where the parts are often produced through casting or by subtractive manufacturing methods. In the case of casting, the material is melted and then poured into a mold to generate the desired geometry [2], [3]. As per subtractive manufacturing a stock material is produced through casting and this stock is then shaped through various means of cutting and removing material, hence the subtractive nature of these processes [4].

The implementation of AM technology in industry has grown significantly in past years as these methods offer many benefits which include reduction of waste material, freedom of design, and rapid prototyping, to name a few [5], [6]. According to designation F2792 of the American Society for Testing and Materials (ASTM), there are seven AM process categories [7]. One technology that has gained much recognition in its advancements in various fields and industries is Powder Bed Fusion (PBF).

1.1.1 Overview of Laser Powder Bed Fusion

As per the previously mentioned standard, Powder Bed Fusion refers to "an additive manufacturing process in which thermal energy selectively fuses regions of a powder bed [7]." The thermal energy required to fuse the powder material is generated by either an electron beam or a laser. The schematic represented in Figure 1.1 illustrates how the process functions when the heat source is a laser. In order to differentiate between the two forms of PBF, the latter method is often referred to as Laser Powder Bed Fusion (L-PBF).

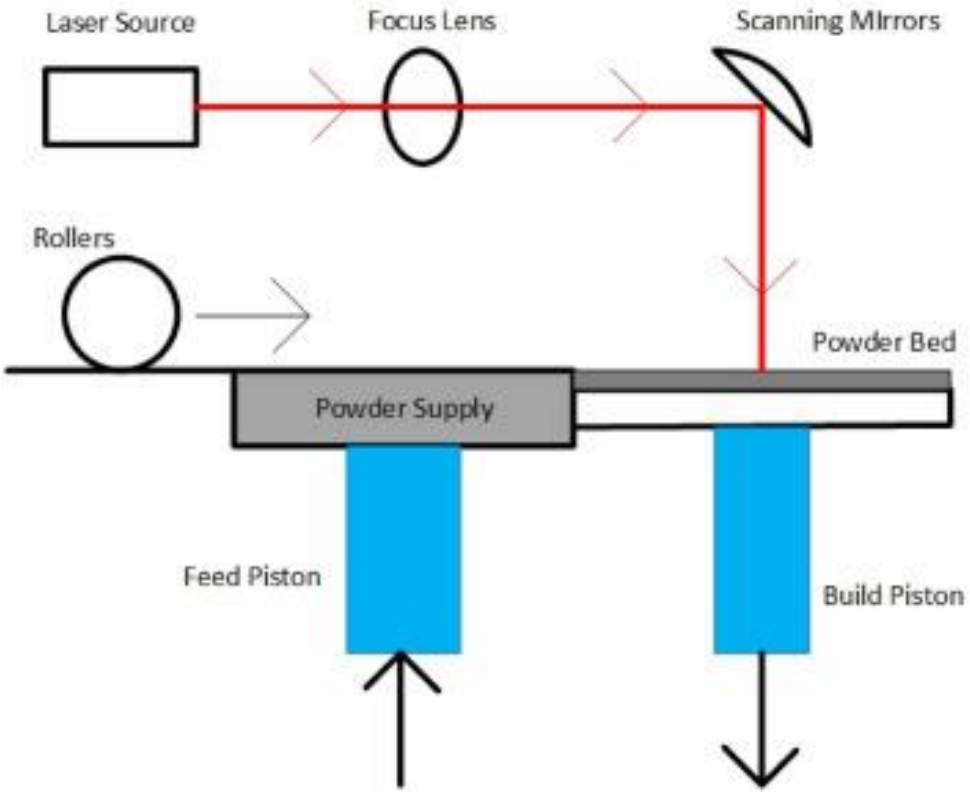

Figure 1.1 Schematic of L-PBF System [8]

L-PBF has evolved significantly since it was first developed by Carl Deckard and Joseph Beaman in 1986 at The University of Texas [9], [10]. The original machine used a high-powered laser that generated heat energy to fuse powder materials into a 3D object. Thanks to advancements in laser technologies as well as other areas, today's L-PBF systems are capable of working with an array of materials spanning from polymers to metals to ceramics and composites [8], [11].

The general feedstock for this process as the name suggests is in the form of powder material. The layout of the machine varies between systems however, certain features are represented in similar manners throughout these units. These features include the laser source, the optical equipment (lenses and mirrors), the powder bed situated on the build platform, a powder supply/reservoir, and a powder distribution mechanism (roller, rake, etc.).

Generally, the process steps are as follows. First, a new layer of powder is evenly distributed along the bed. Second, the laser is maneuvered by the mirrors in order to fuse powders at desired locations on the powder bed. Once, the laser completes its pass on the first layer, the build platform lowers, and a new layer of powder is introduced. The laser then comes in and fuses the desired areas once more. The process is repeated until the build is complete.

1.1.2 Challenges of L-PBF

Because of the various intricacies of the L-PBF process many challenges arise when using this technology. To ensure the quality of the components placed into the various industries serviced by this process, these challenges must be addressed. These challenges include the formation of common defects including, but not limited to balling, porosity, high surface roughness, and the presence of residual stress which can lead to distortion and cracking [8].

1.1.2.1 Balling

Balling can occur for two main reasons, the first can be explained as the result of loose powders on the powder bed [12]. The accumulation of these powders is then exposed to the heat energy of the laser process which rather than fuse into a smooth layer, the powder balls up due to the material's tendency to achieve a low state of surface energy. The second reason does not have to do with the presence of loose powders, but rather with the inability for the powder to fuse with the substrate or previous layer [13], [14], [15], [16]. The culprit in this case may be inadequate contact between the two, however the balling phenomena is present due to a similar understanding of the principle of minimum surface energy. In this case the balling effect occurs due to surface tension. Figure 1.2 and Figure 1.3 demonstrate commonly reported cases of balling present in L-PBF.

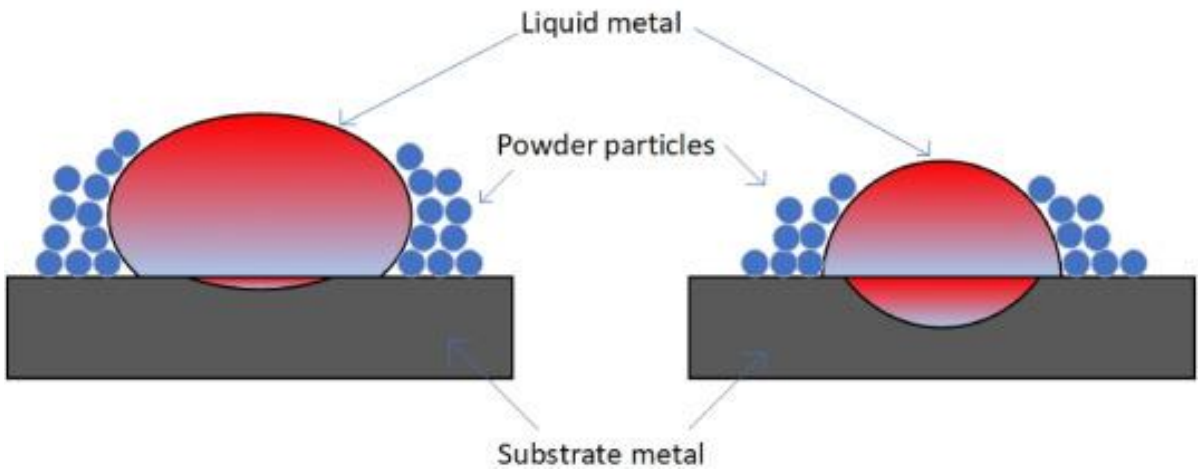

Figure 1.2 Balling with less (left) and more (right) molten substrate [8]

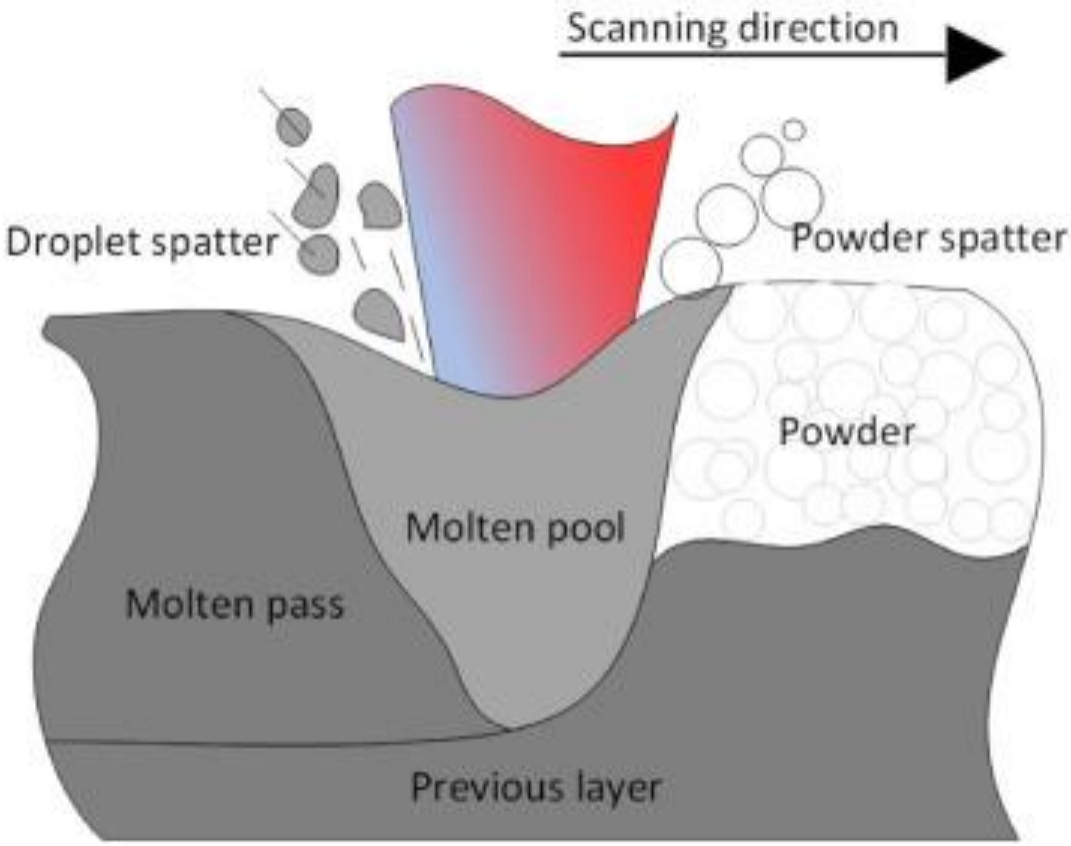

Figure 1.3 Balling due to droplet spatter [8]

The presence of this defect can be detrimental to this AM process [17], [18]. When balling occurs throughout the build, it can severely affect the quality of newly spread layers of powder which could lead to voids in the part being produced. Furthermore, the balling effect is often taller than the layer which can become an obstacle for the rake or roller often damaging this mechanism when they come in contact. When balling occurs on the final layers of a build, the surface quality of the print is also compromised.

1.1.2.2 Porosity

Porosity can be thought of as voids or cavities within a particular component. In the L-PBF process, porosity can be classified into the three types of pores that are formed when inadequate parameters are utilized. These include fusion pores, gas pores, and shrinkage pores named for the mechanisms behind their respective creations [19], [20], [21].

Fusion pores occur when there is not enough energy produced to join the current layer to a the layer below [21]. This lack of energy prevents proper melting between the layers, resulting in a gap being formed. If this is not corrected during the build, the resulting build while have a large quantity of fusion porosity or lack of fusion.

Gas pores can also be thought of as fusion pores; however, the main culprit here is not the lack of energy but rather the presence of gases. This gas may become entrapped during the build, creating a barrier between layers, ultimately denying the possibility for the layers to fuse as they solidify [22]. Eventually, the gas escapes leaving behind a cavity in its place. Because of the nature of the formation of these pores, gas pores tend to more spherical than fusion pores [23], [24]. Figure 1.4 illustrates the difference between fusion pores and gas pores.

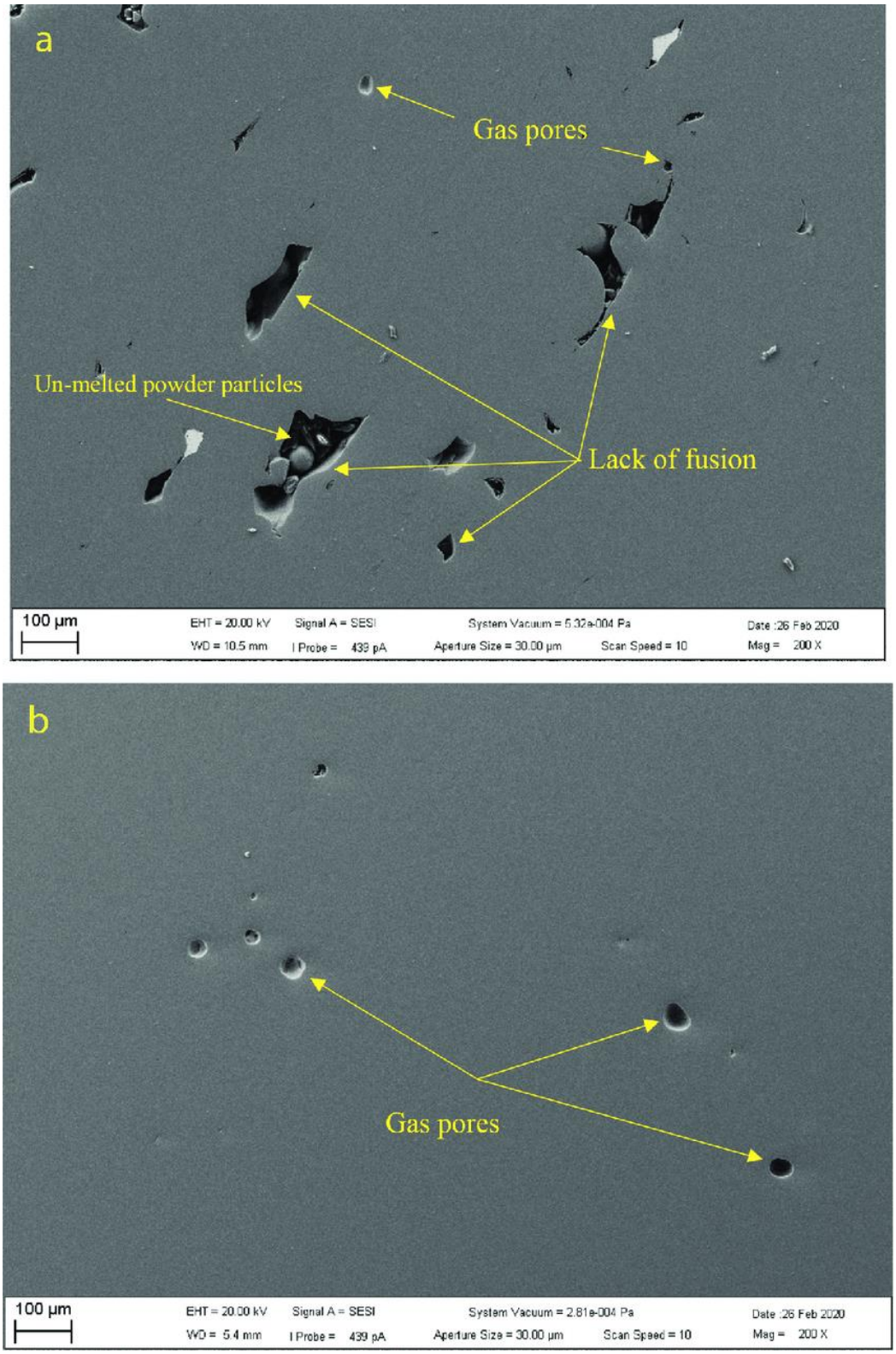

Figure 1.4 a) Irregular shaped fusion pores b) spherical gas pores [25]

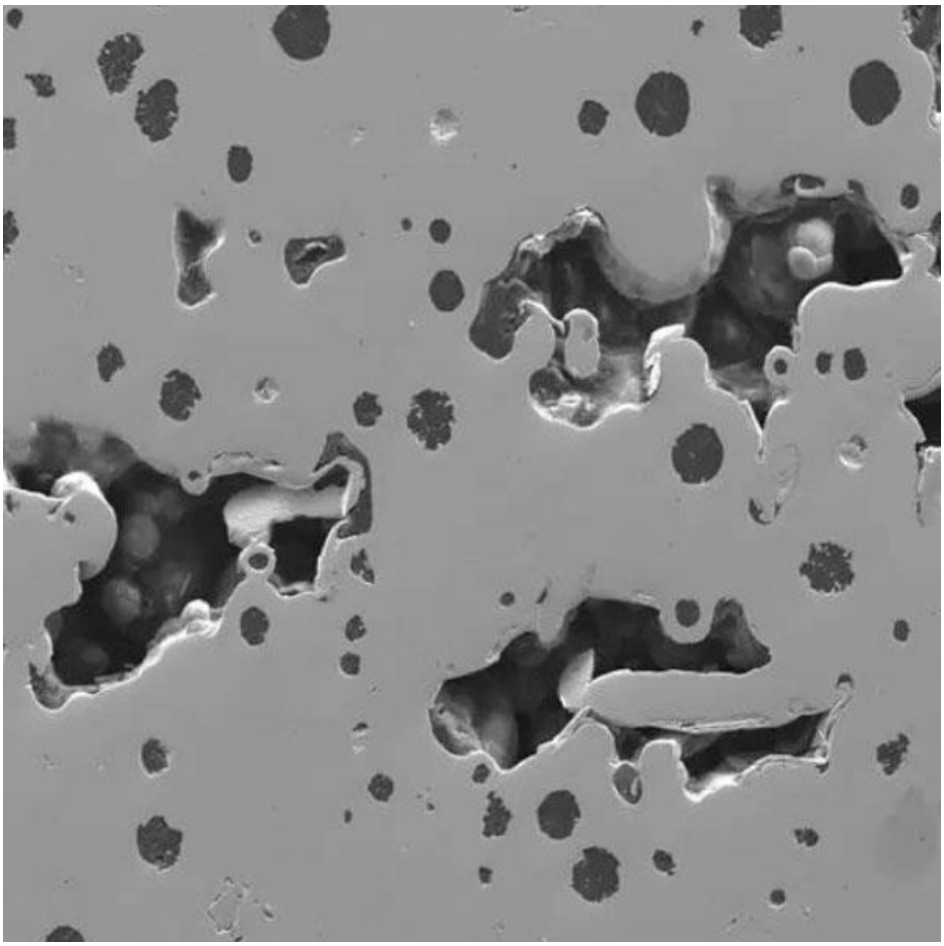

Figure 1.5 Shrinkage porosity in a cast part [26]

Lastly, shrinkage pores are generated during the solidification of the molten layers. These are a result of insufficient molten material. Because there is not enough material, the material shrinks as it solidifies creating voids [27]. Figure 1.5 demonstrates how this porosity looks in a cast metal part.

Porosity is a major defect that is not exclusive to the L-PBF process. Ideally, the goal of any manufacturing process is to achieve a fully dense part, in other words, the absence of porosity. Although this may not be entirely feasible in practice, certain steps can be taken to achieve highly dense builds.

1.1.2.3 High Surface Roughness

High surface roughness is a concern because it can greatly affect the quality of the component produced through L-PBF. The roughness of a part is often correlated with the magnitude of the diameter of the powder being used, i.e. finer powders produce parts with finer surface finish [8]. Unfortunately, these powders are often much more difficult and expensive to produce and handle.

Roughness is also attributed to oxidation that results from atmospheric gases present in the build chamber combined with the adhesion of partially melted powders [28]. L-PBF is therefore operated in an inert environment to reduce some of these defects. However, postprocessing techniques have been needed to achieve desired surface quality.

1.1.2.4 Residual Stresses

Residual stresses are formed because of the rapid heating and cooling nature of the L-PBF process. When the laser is focused on to the powder, it quickly adds a lot of heat energy in order to fuse the layers. The subsequent layer of powder that is added is significantly colder than what was previously melted. This large thermal gradient that is created in a relatively short period of time is what causes L-PBF parts to have residual stresses [29], [30].

These internal stresses can be catastrophic as they can lead to deforming or cracking the parts in order to relieve the stresses [31]. These stress may seem to be a norm of the L-PBF process that one may be forced to accept, however, Shiomil et al. found approximately 55% and 40% reduction in residual stresses due to remelting tracks and preheating the substrate [32].

1.2 SURFACE QUALITY

Regardless of how you manufacture any part that is to be utilized in the real world, it is essential that a favorable surface quality is achieved. Before one can take steps to ensure that the surface finish is acceptable, one must understand how the surface quality is observed, reported, and ultimately altered.

1.2.1 Roughness Measurement Techniques

When it comes to specifying the various forms and machines used to measure the roughness of a material or a specific part, it ultimately comes down to two measurement techniques, contact and non-contact [33], [34]. As the name suggests, the first technique deals with some sort of physical contact made by a stylus typically made of a diamond tip which moves across the surface. As the stylus moves through the surface, it creates a map of the surface noting the changes in height and quantifying them at quite an impressive scale.

This “map” of the variations in height is then passed through some filter that cuts away excess or erroneous data. The resulting value is the representative roughness of the surface, typically represented in microns. This manner of evaluation is highly accepted in industry, however certain questions arise with this method. Because of the physical nature of this process, it is often difficult to reproduce the measurements. It is also important to note that because the stylus is often equipped with the diamond tip, the profile that is tested is essentially scratched and may have some effect on the quality of the surface. Figure 1.6 demonstrates the typical operation of a contact roughness measurement device.

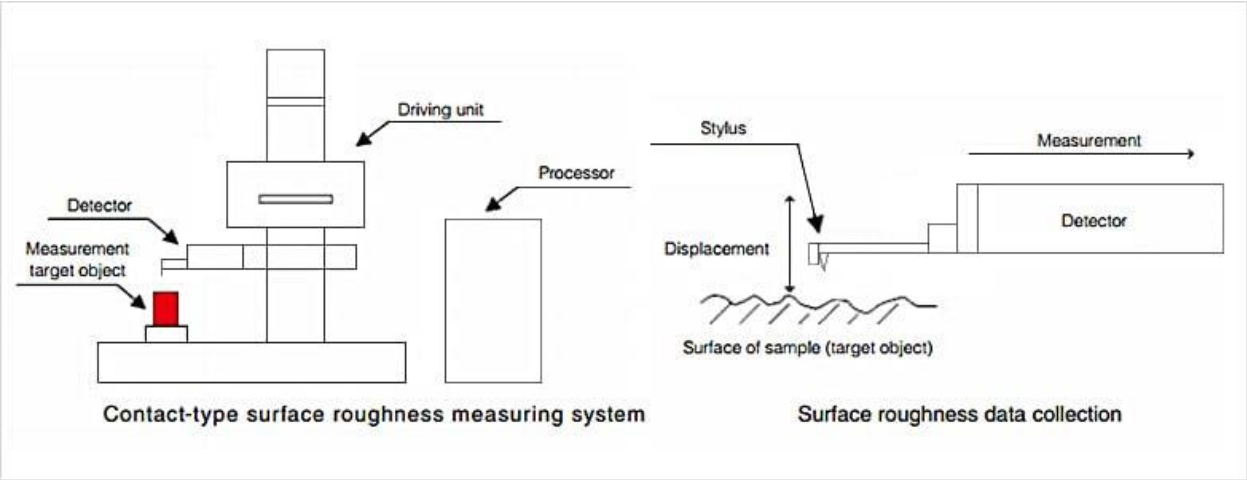

Figure 1.6 Schematic of contact surface roughness measuring system [35]

Because of this and other factors, non-contact forms of measuring the surface roughness of components has been growing in popularity and is quickly being adopted in industry [33], [36]. The most prolific of the non-contact methods would have to be optical measurement techniques. As the name suggests, this method uses the behavior of light in order to map the surface [37]. This method is rather quick, as the equipment can quickly scan a large area or multiple parts at a time. Again, this data is filtered, and the roughness of the specimen is given.

Although it may seem that optical means of analyzing the surface is superior to mechanical/contact forms of analysis due to the ease of inspecting the same area fairly easily without altering said surface [38], this method still faces some issues. Most notably would be the sensitivity of this technique when scanning relatively smooth parts. Typically, smooth surfaces tend to be more reflective as noted by their

shiny exterior. This can be a problem as optical measurement techniques rely on the reflection and refraction of light, which on a smooth surface the readings may produce erroneous data or may even fail to recognize the specimen [33]. Figure 1.7 illustrates a schematic of the general operation and the components of an optical roughness measurement device.

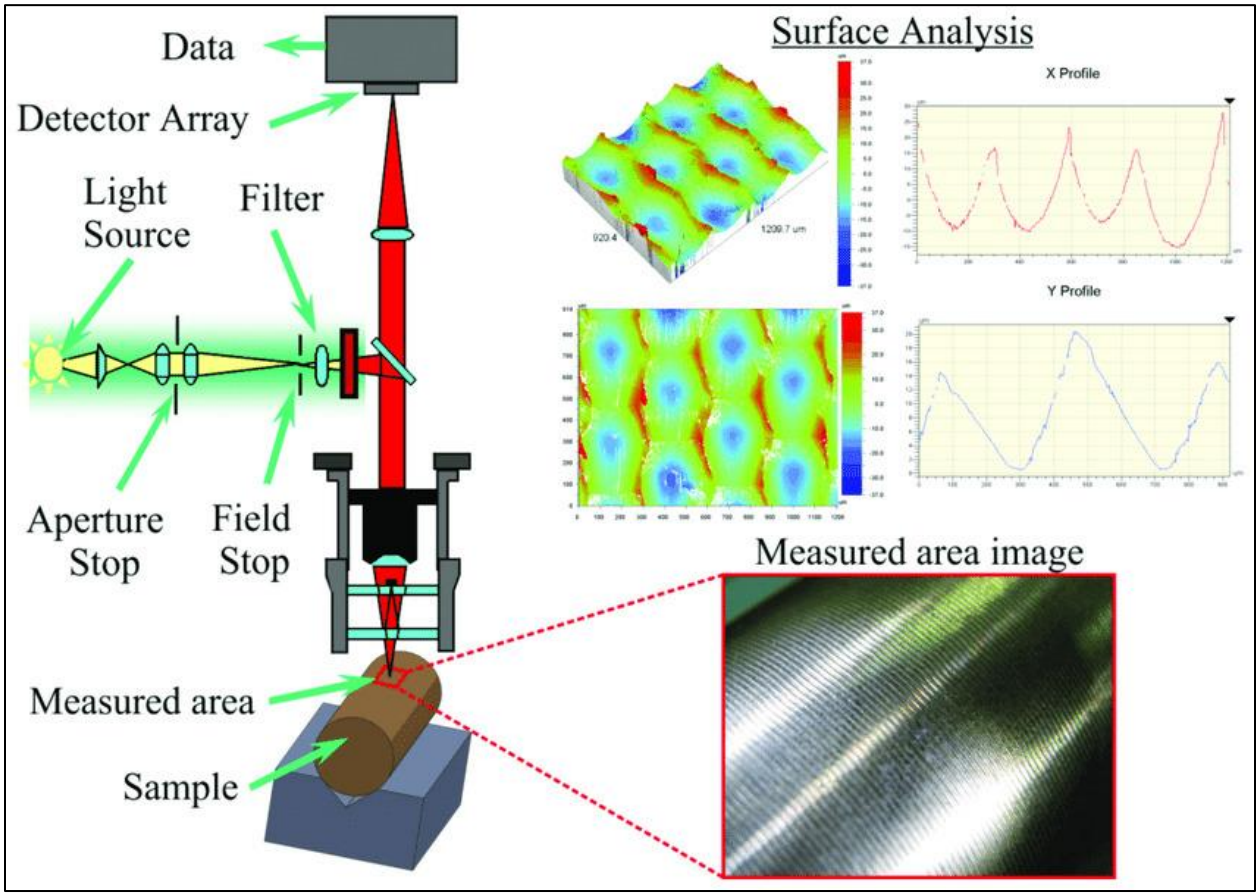

Figure 1.7 Schematic of optical roughness measurement device [39]

Both forms of analyzing roughness have both their advantages and disadvantages, but it is important to recognize their strengths and weaknesses in order to be certain that the data produced can be accepted. Regardless of the measuring method that is used, it is important to follow the standard for measuring specific to your needs and applications.

1.2.2 Roughness Measurement Parameters

When it comes to the different measurement parameters for roughness, they can be split into two main categories. The first category is line or trace roughness, which is denoted by a capital 'R' and followed by a subscript that denotes the method used to quantify the roughness. The second category is surface roughness measured over an area, which is denoted by a capital 'S' and is also accompanied by a subscript. Although there are advantages and disadvantages when comparing the roughness values between line and surface area, the characterizing feature that is essential to observe would be the parameter denoted by the subscript. Figure 1.8 shows some of the most common parameters used when analyzing roughness along with a brief description of what each parameter specifies and how it is calculated.

Symbol	Name	Equations	Description
R_a, S_a	Arithmetic average	$S_a = \frac{1}{MN}\sum_{j=1}^{N}\sum_{i=1}^{M}\left\|\eta\left(x_i, y_j\right)\right\|$	Average of |z|
R_q, S_q	Root mean square (RMS) roughness	$S_q = \sqrt{\frac{1}{MN}\sum_{j=1}^{N}\sum_{i=1}^{M}\eta^2\left(x_i, y_j\right)}$	Standard deviation of z
R_p, S_p	Maximum height of peaks	$S_p = MAX\ (\eta_p)$	Max z
R_v, S_v	Maximum depth of valleys	$S_v = MIN\ (\eta_v)$	Min z
R_z, S_z	Maximum height of the surface	$S_z = (\|S_p\| + \|S_v\|)$	Max z- Min z

Figure 1.8 Common roughness parameters [40]

The most widely used roughness parameters are R_a and S_a [41], [42]. The 'a' in the subscript signifies the arithmetic mean or average z-value of the analyzed surface [40], [41], [43], [44]. For R_a, this would be the average height of the z-profile measured along a line with respect to an arbitrary reference line. For S_a, this would be the average height of a specified area with regards to an arbitrary reference plane. These methods of reporting roughness are widely used in industry and academia as they offer a quick and rather intuitive explanation of the overall average roughness of a part or specimen.

Other widely used roughness parameters are R_q and S_q. The 'q' in the subscripts describes that the standard deviation of the z-profile is what is being reported by these two parameters. These are often referred to as the quadratic mean or root mean square (RMS) average deviation [40], [41], [45]. For R_q, this would be the calculated deviation in the height with respect to the mean line. For S_q, it would

represent the average deviation from the average profile plane. These parameters help demonstrate whether the surface is uniform or not.

Next, there is roughness parameters R_p and S_p. The 'p' in the subscript stands for the peak z-value. Given this, it is understood that the parameter signifies the maximum height within the sampled region [40], [41]. For R_p, this would be maximum z-value within a single sampling length. To report the average R_p of a part, it would be necessary to average the R_p value over the assessment length. For S_p, this would be maximum z-value within a single sampling area. These parameters are useful when combined with R_a and S_a. If there is a large discrepancy between the peak roughness and average roughness, this could signal problematic surface deficiencies.

On the other side of the spectrum are roughness parameters R_v and S_v. The 'v' in the subscripts stands for the valley z-value. The valley is the maximum negative height or maximum depth [40], [41], [42]. For R_v, this would indicate lowest z-value within the sampling length. For S_v, it would be the lowest z-value within the sampling area. Determining the lowest valley depth on a component may be crucial to understanding the performance of said object. These valleys tend to act as surface defects which essentially reduce the feature size resulting in stress concentrating at this location. These locations can therefore, be seen as failure initiation sites when the parts are loaded with a stress [44], [46], [47].

Lastly, there are roughness parameters R_z and S_z. The 'z' in the subscript denotes that the given roughness parameter describes the maximum height of the surface [40], [41], [43]. That is to say, you take the minimum z-value and subtract it from the maximum z-value. Note that because these are taken from a mean reference line, the minimum value would be negative. Another way of calculating this height would be to sum the absolute values of the maximum peak and valley.

1.2.3 Surface Finishing Techniques

As previously noted, one of the challenges of L-PBF technologies is the high surface roughness; in order to combat the possible issues associated with the high surface roughness, steps can be taken to improve the quality of said surface. There are numerous methods to improve the surface finish, however, some techniques are not as readily available due to factors such as cost, lead times, or simply availability. Some common techniques though are milling, grinding, polishing, and the use of abrasive media blasting such as sand blasting. The latter has many forms and is growing in popularity among post processing techniques of AM parts due to its capability of servicing complex geometries.

Milling is a widely used machining technique. This process has many forms depending on the desired outcome or cutting approach [48], [49]. Generally speaking, this process can be described by the use of rotary cutters to remove

material from the workpiece [50]. Figure 1.9 illustrates a general form of milling. Due to the rotary nature of milling as the tool moves across the surface, ridges are left behind. The presence of these ridges is a regular occurrence when using this machining method. The distance between and height of the ridges are dependent on the cutting parameters which if not properly controlled, can lead to significant variations on the surface finish [50], [51].

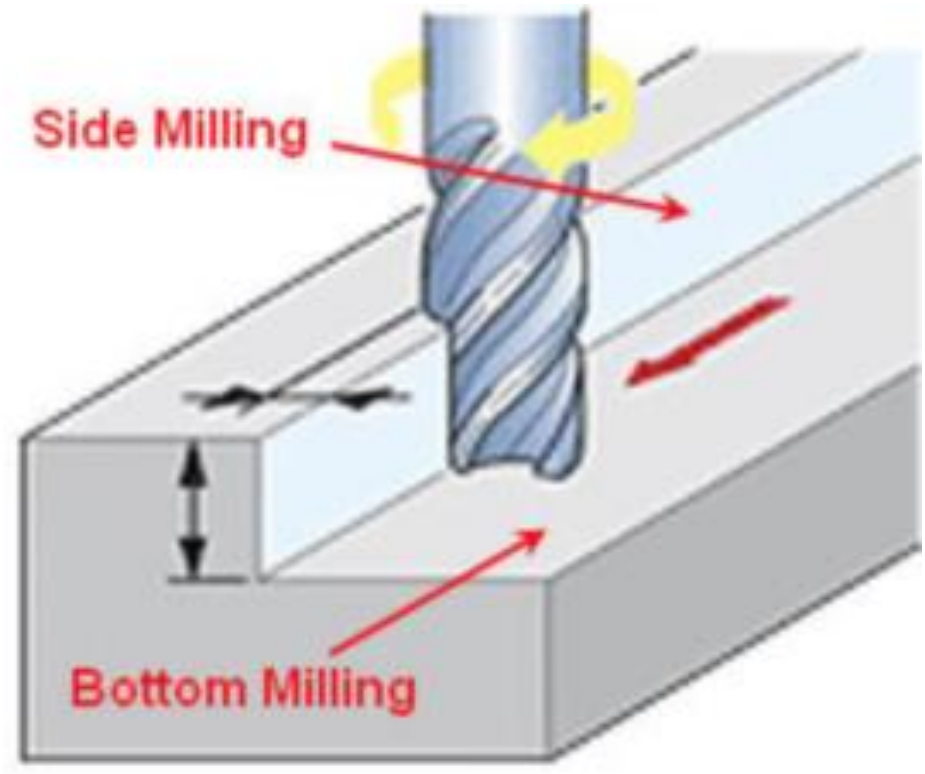

Figure 1.9 Visualization of milling [52]

Grinding, or abrasive cutting is another widely used machining technique. The primary use of this technique is to improve the surface quality of the workpiece. Grinding can be seen as microscopic cutting; the process essentially removes material at a small scale. This abrasive machining process typically uses a grinding wheel as the cutting tool; the grinding wheel is and expendable part made from a matrix of coarse abrasive particles [53]. Figure 1.10 demonstrates the general operation of a grinding wheel. The makeup of the grinding wheel however can lead to inconsistent contact to the workpiece due to wearing which can lead to "inconsistent surface quality and low processing efficiency [54], [55], [56], [57].

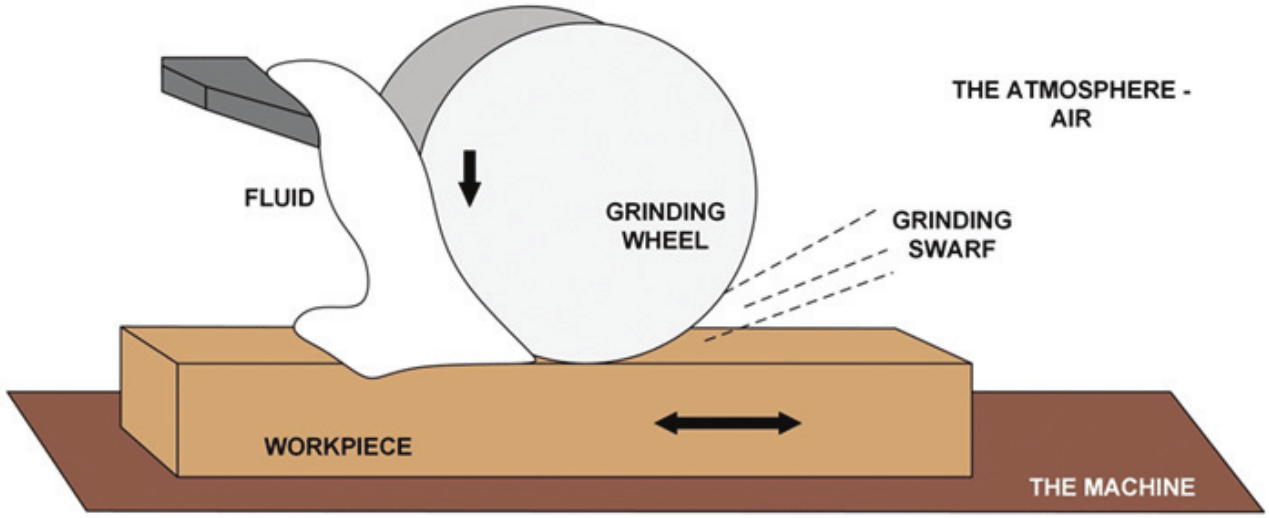

Figure 1.10 Diagram of the grinding process [58, p. 1]

Polishing is a finishing process used to create a smooth surface. Typically, the polishing process consists of an abrasive that is glued to a work wheel [59]. The work wheel is then passed over the work piece to remove any imperfections on the surface. Figure 1.11 illustrates how a workpiece is polished. This is typically a multi-stage process as the polishing pad or work wheel is swapped out for a wheel with a finer abrasive at each subsequent step. It is important to note that a polished surface does not need to have a mirror-like finish.

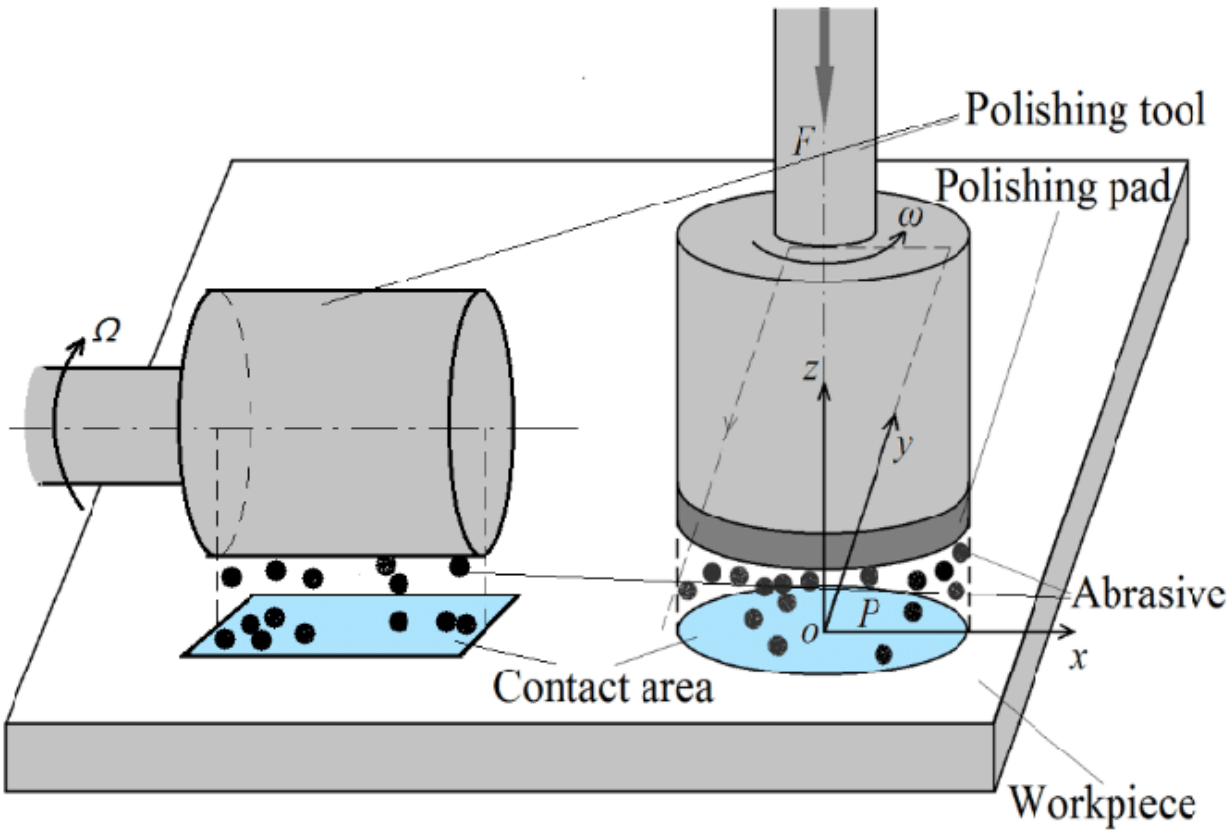

Figure 1.11 Schematic of polishing methods [60]

Abrasive blasting is the process of propelling an abrasive media under high pressure to the workpiece. This can be done for several applications: to smooth a rough surface, to roughen a previously smooth surface, or to shape the surface or remove contaminants [61]. Figure 1.12 demonstrates the general operation of abrasive blasting.

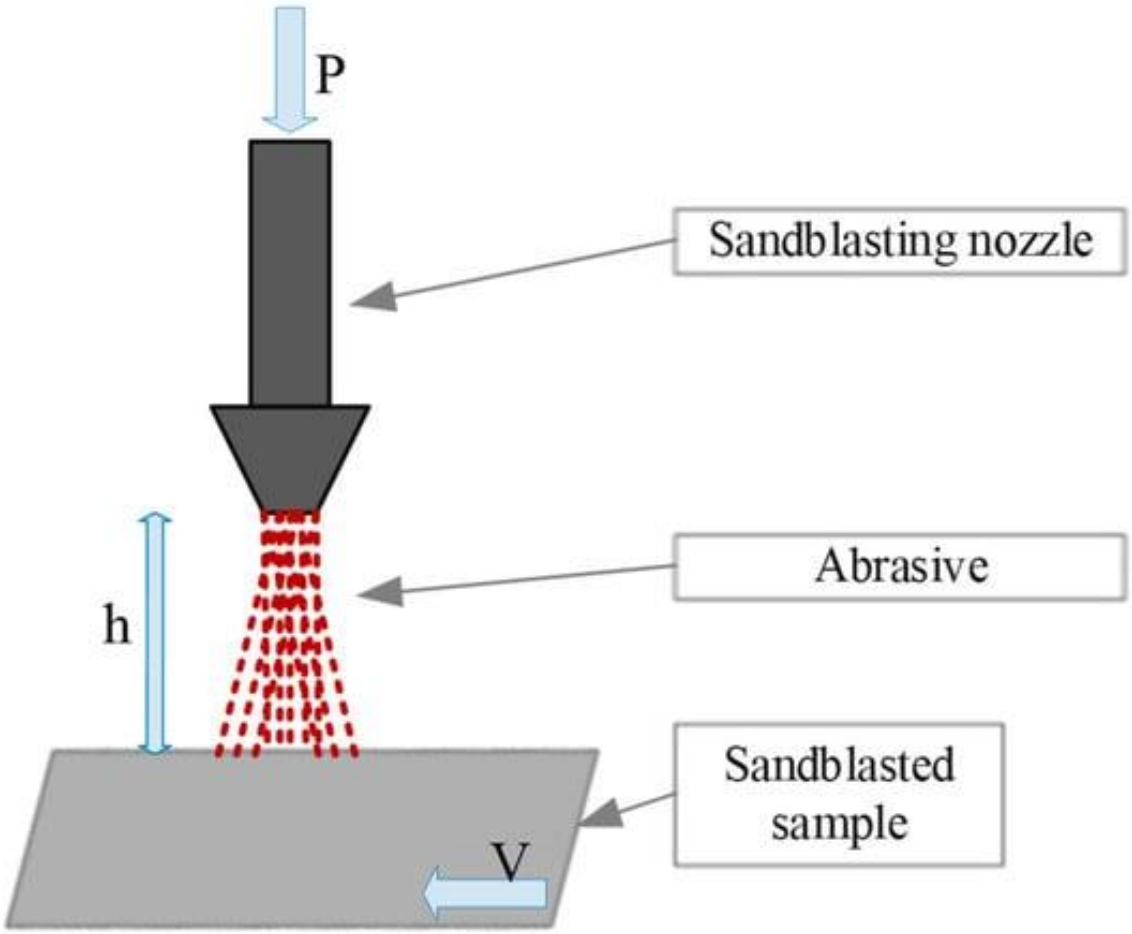

Figure 1.12 Sandblasting diagram [62]

1.3 FATIGUE TESTING

Fatigue testing is a crucial form of mechanical testing; it is performed by applying cyclical loading to a specimen [63]. These tests help determine the fatigue life of a material, or the operational life of a component that is expected to be susceptible to fatigue. Fatigue tests can be applied to full size, operational components however, test coupons are typically used. These coupons are either subjected to uniaxial or flexural fatigue.

The fatigue performance, like other mechanical properties is a primary concern for aerospace structures [64]. It has been demonstrated that the fatigue endurance of AM materials such as Ti-6Al-4V, is comparable to that of wrought materials [65], [66]. However, these components are also affected by issues associated with AM such as surface conditions [32], [65], [66], [67]. Post processing techniques like machining have also been shown to impact the fatigue performance of these AM parts [65], [66], [67], [68].

1.3.1 Uniaxial Fatigue Testing

Uniaxial fatigue testing is the standard practice for strain-controlled fatigue testing as per ASTM E606 standard [69]. In this form of testing, the specimen is subjected to cyclical loading in a single axis, hence the name, uniaxial. The load amplitude typically ranges from a maximum tensile stress to a maximum

compressive stress. The test geometry as defined by the standard is in the shape of an hourglass, similar to that of a tensile test specimen. Because of this geometry, the coupon is expected to fail along the gauge diameter. Figure 1.13 demonstrates the experimental setup for a uniaxial fatigue test.

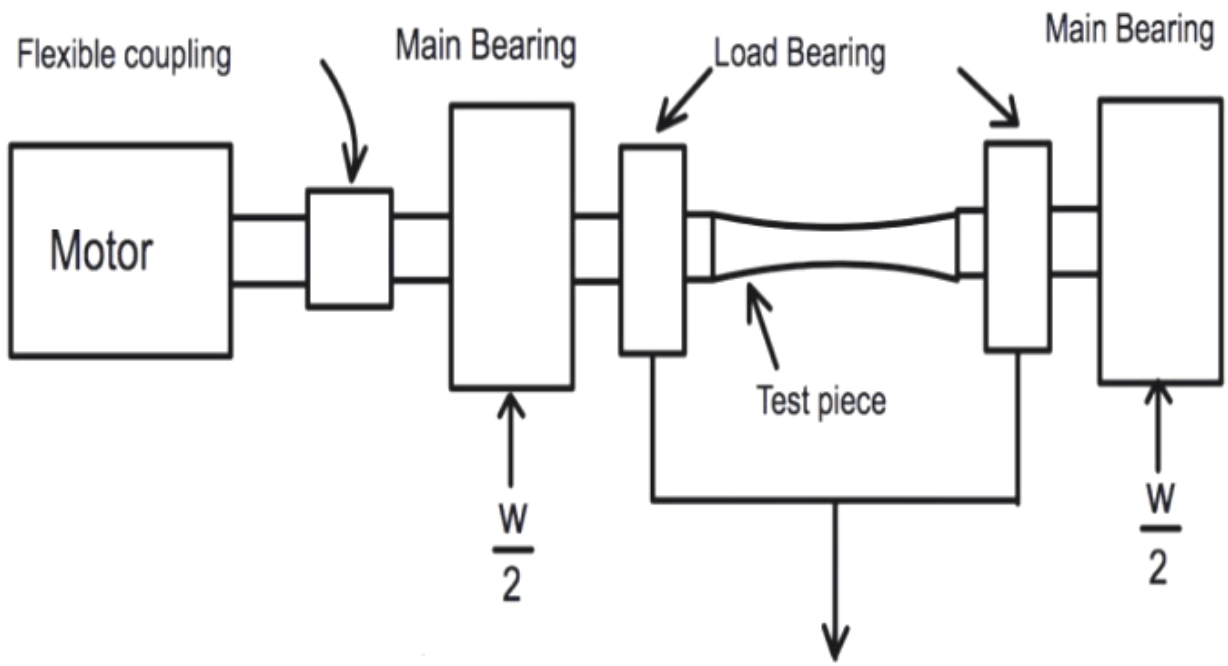

Figure 1.13 Uniaxial fatigue test setup [70]

An overwhelming majority of fatigue studies on AM parts focus on uniaxial fatigue testing [44], [71], [72], [73], [74], [75]. However, there are concerns that the single axis testing may not be representative of real-world stresses which has led many to perform multiaxial fatigue tests in an attempt to replicate these end-use scenarios [76], [77], [78], [79], [80], [81].

1.3.2 Flexural Fatigue Testing

Flexural fatigue testing is the bending fatigue testing mechanism for rigid and semi-rigid plastics as defined by designation D7774 of the ASTM standards [82]. There are two main procedures described under this designation. The first is a three-point bending test in which a rectangular test specimen is held at three locations and is then subjected to tensile and compressive cyclical loading. The second method is a four-point bending test similar to the previous with an added holding location. Figure 1.14 highlights a typical four-point bending test setup.

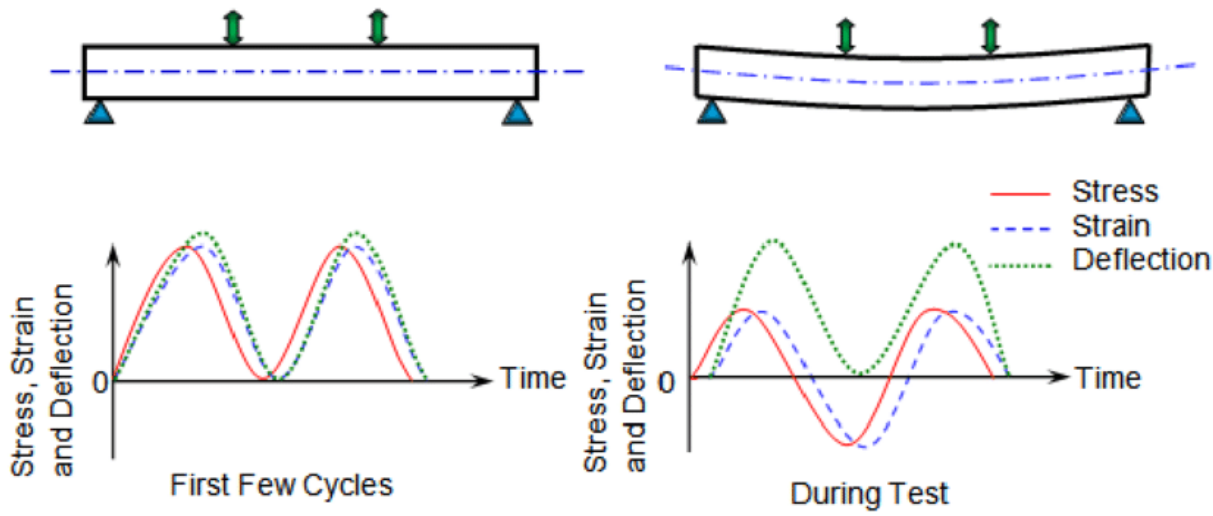

Figure 1.14 Four-point bending test setup [83]

Flexural fatigue testing allows for a more accurate model of expected in use loading conditions and has been increasingly adopted as a form of qualifying materials [84], [85], [86], [87], [88], [89]. This method needs to be further examined to determine its applicability and significance when analyzing metal components.

1.3.3 Fracture Surface

In the study of fatigue specimens, a thorough analysis of the fracture surface is essential. The fracture surface serves as a critical gateway to comprehending the underlying reasons for part failure. Accurate inspection and interpretation of fracture features are imperative for informed assessments [90], [91].

One of the primary pieces of information that can be obtained from the fracture surface is the material properties, namely whether the material is ductile or brittle [92]. In a ductile material, dimples can be seen throughout the fracture surface as evidence for its plastic instability [93], [94], [95]. In a brittle material, the fracture is relatively flat with crystalline facets [96], [97]. Figure 1.15 and Figure 1.16 highlight a ductile and brittle fracture surface, respectively.

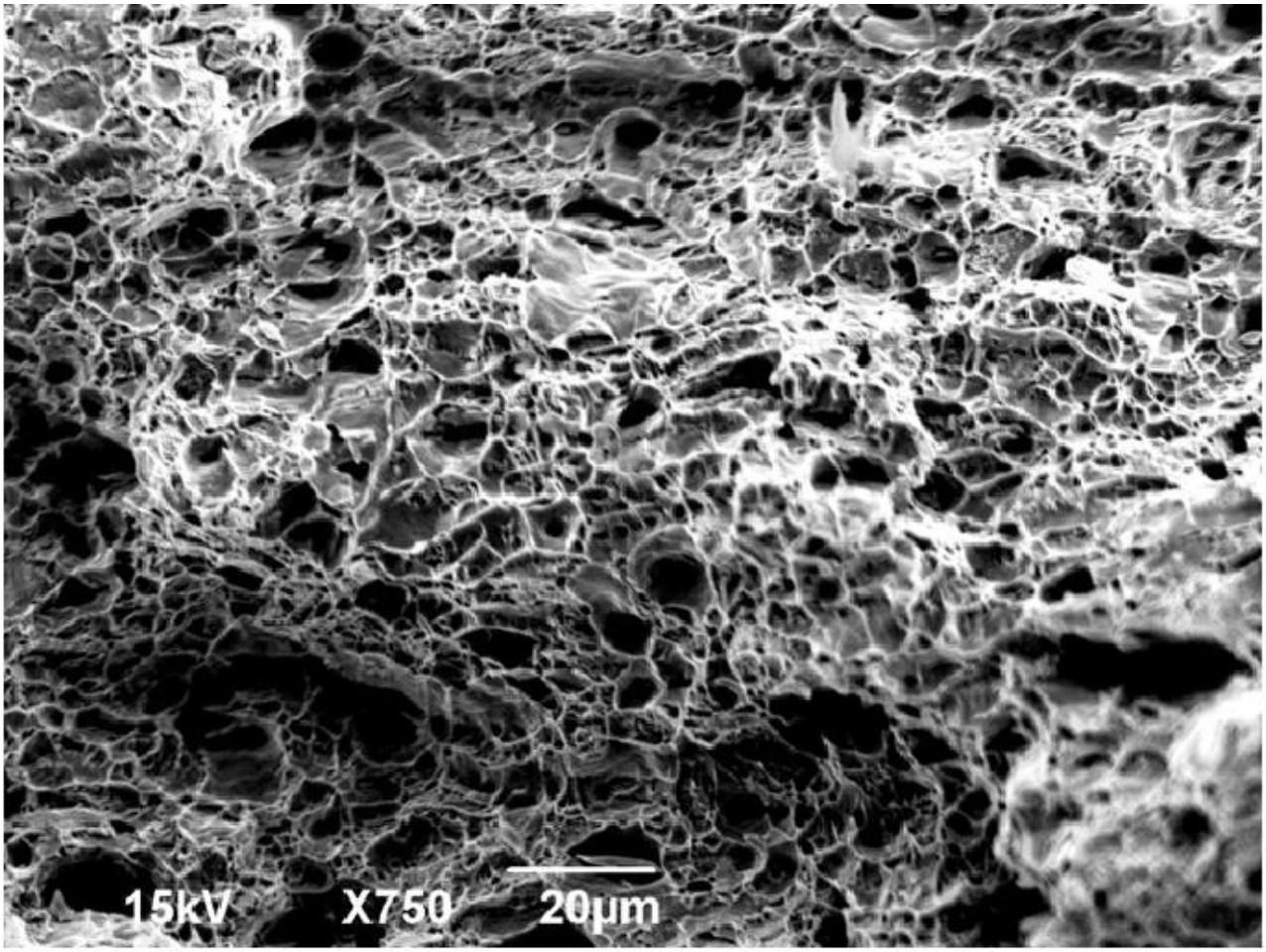

Figure 1.15 Image of ductile fracture surface [98, p. 10]

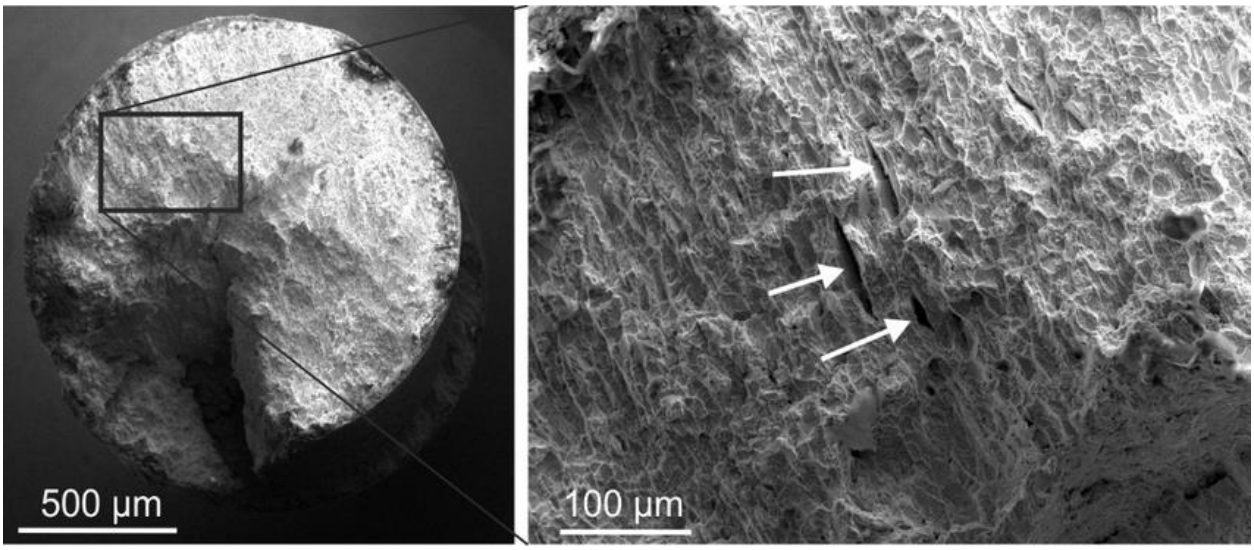

Figure 1.16 Image of brittle fracture surface [99, p. 33]

The fracture surface typically has two main regions: the fatigue or crack growth region and the overload region [90], [91]. The fatigue region is a rough surface that experiences gradual progression as evidenced by beach marks and striations on the surface. In contrast, the overload region experiences sudden catastrophic failure with little to no deformation evident on the surface.

Chapter 2: Materials and Methods

2.1 Powder Morphology

Grade 5 titanium powder produced by ATI was utilized to produce the specimens. The powder was sampled with regards to designation B215 of the ASTM standards [100] and characterized using a Retsch Technology Camsizer X2 X-Dry following designation B822 of the ASTM standard [101]. As demonstrated in Figure 2.1 the powder demonstrates a spherical morphology. According to the analysis of the sampled powder, the feedstock has d10, d50, and d90 of 25, 37, and 49 microns, respectively. This information is shown in Table 2.1.

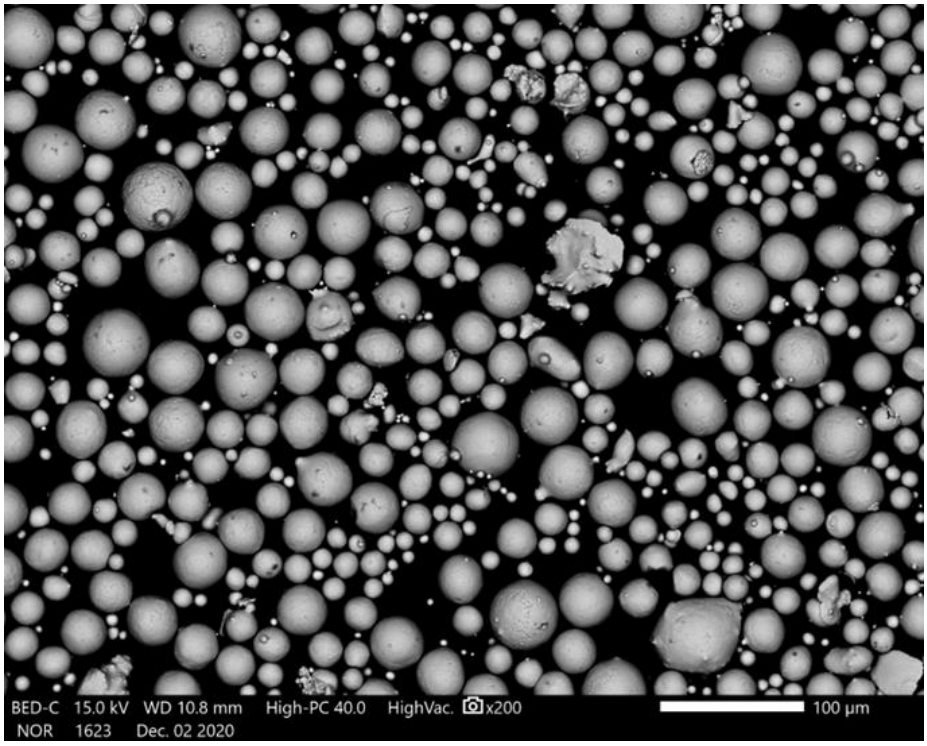

Figure 2.1 SEM of Ti-6Al-4V powder

Table 2.1 Powder analysis data

		by volume			Size Class (by volume)							
particles imaged	Mean particle size	d10	d50	d90	0-10µm	10-20µm	20-30µm	30-40µm	40-50µm	50-60µm	60-70µm	70+ µm
#	µm	µm	µm	µm	%	%	%	%	%	%	%	%
4664	37	**25**	**37**	**49**	0.2	3.7	18	41	30	8	0	0

2.2 PART FABRICATION

Rectangular specimens of dimensions of 6mm x 6mm x 45mm were built using an EOS M290 L-PBF system equipped with two Ytterbium lasers. The specimens were built under EOS Nominal parameters, that is a laser power of 280 W and laser scanning speed of 1200 mm/s as illustrated in Figure 2.2. The specimens were fabricated in an Argon environment with gas flow coming from the top of the build plate and the rake introducing fresh powder from the right as depicted in Figure 2.3. The specimens then underwent a stress relief heat treatment in a vacuum furnace. The temperature rose at a rate of 5°C per minute until it reached 600°C. The temperature was held for two hours, and the samples were then evenly cooled at a rate of 5°C per minute.

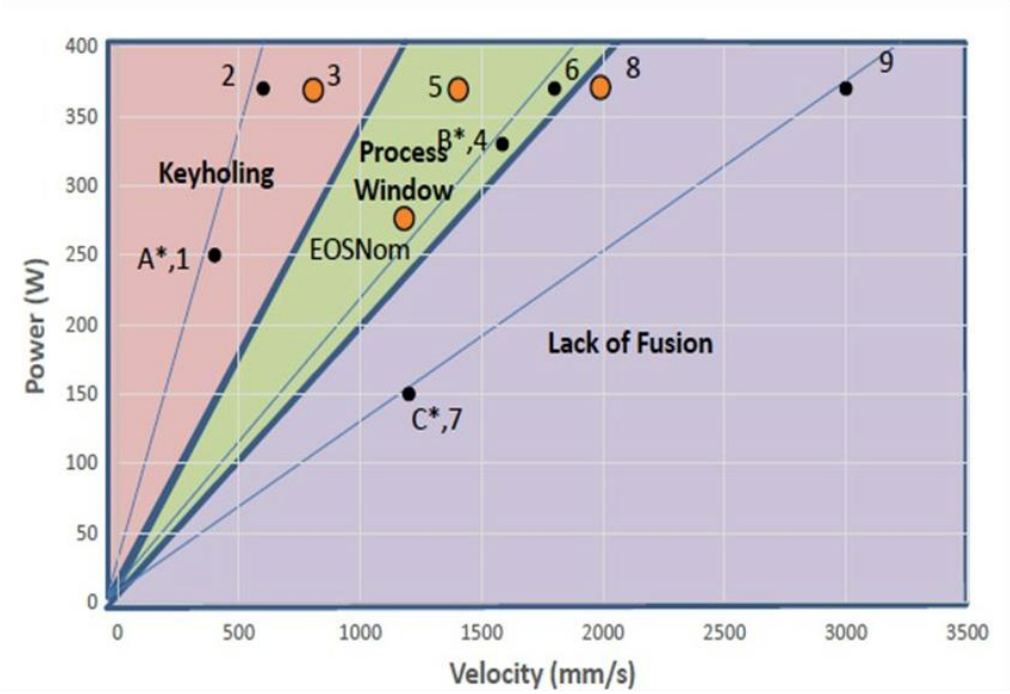

Figure 2.2 EOS P-V diagram for Ti-6Al-4V

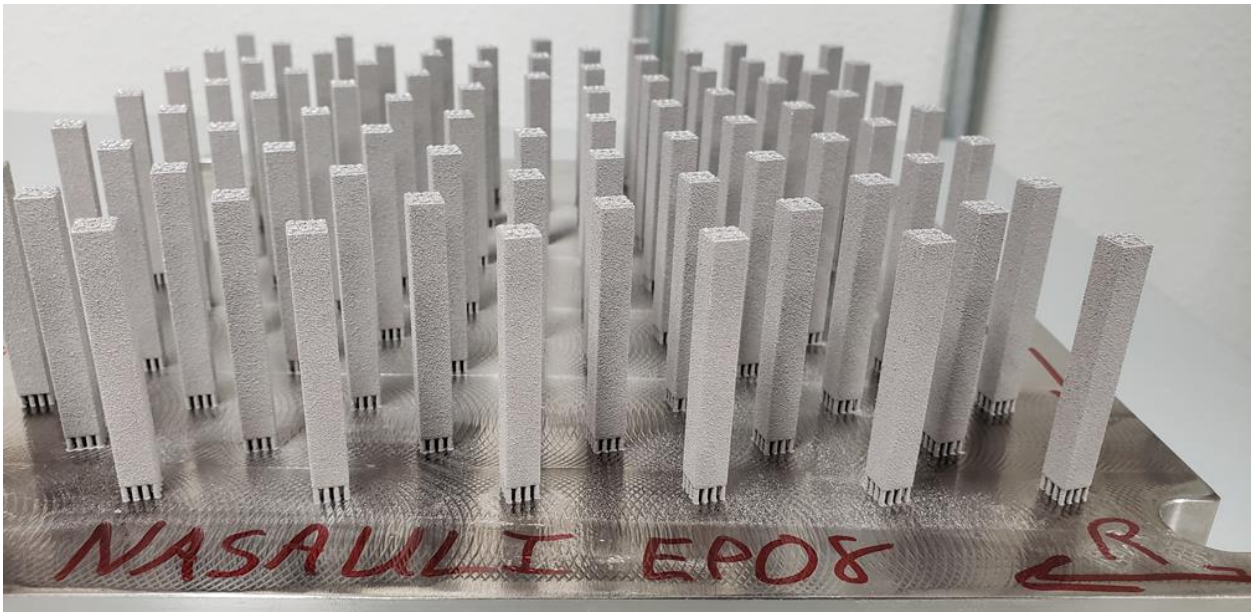

Figure 2.3 Image of completed build

2.3 MACHINING TECHNIQUES

The specimens were randomly assigned to one of four machining techniques to achieve a desired geometry of 5mm x 5mm x 45mm. These include processes that are commonly available such as milling, surface grinding, and polishing as well as thermal atomized fusillade (TAF), a technique specifically designed to improve the quality of complex geometries that are additively manufactured. It is also important to note that the supports were cut off and a 45° chamfer was added to the edges that run along the build direction.

The milled specimens were machined at the UTEP machine shop with an end mill. Figure 2.4 outlines the cutting parameters used. The specimens were milled along the build direction with a single pass, removing 0.5mm from each side. The edge of the cutter remained tangent to edge of the surface. Figure 2.5 depicts the surface of a milled specimen; the ridges produced by this machining technique are clearly visible.

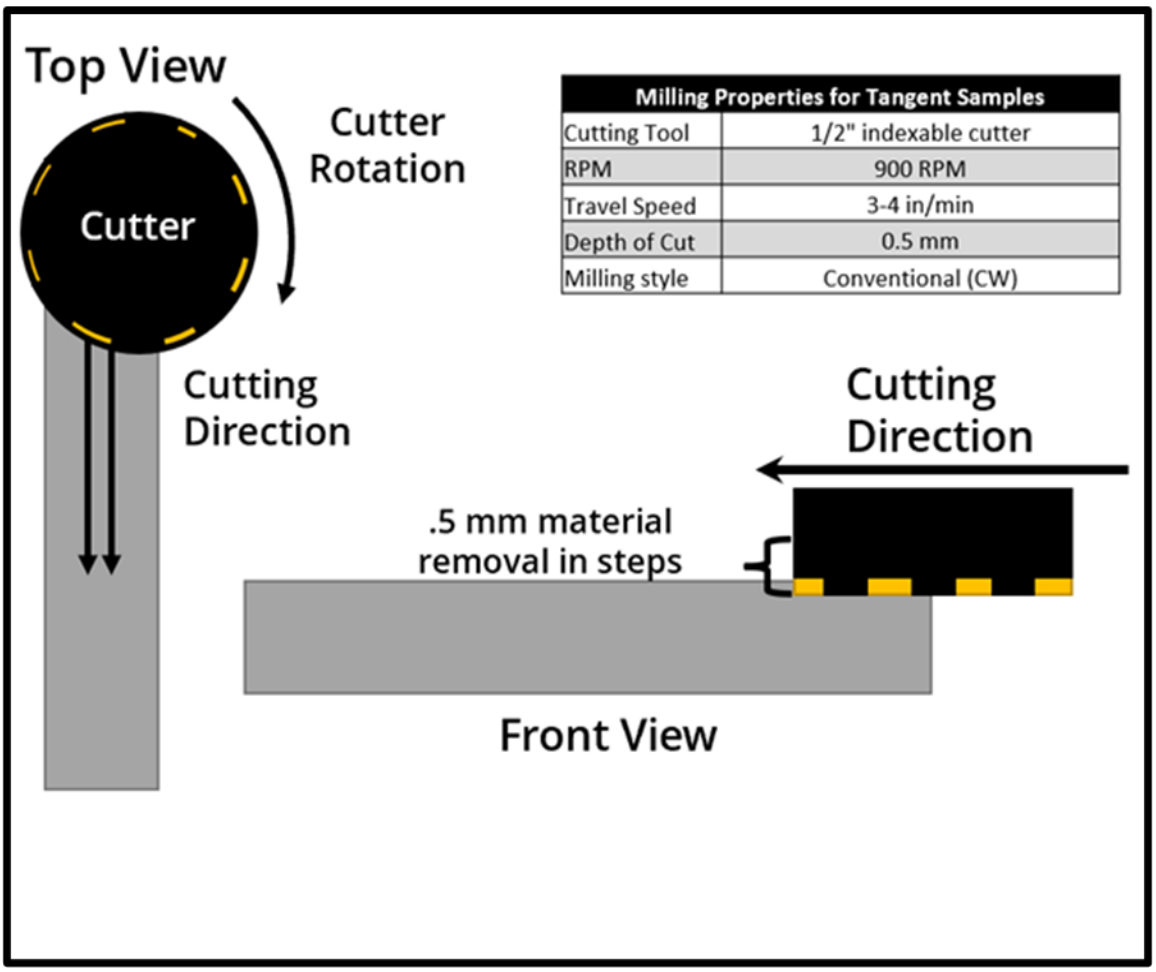

Milling Properties for Tangent Samples	
Cutting Tool	1/2" indexable cutter
RPM	900 RPM
Travel Speed	3-4 in/min
Depth of Cut	0.5 mm
Milling style	Conventional (CW)

Figure 2.4 Cutting parameters for milled specimens

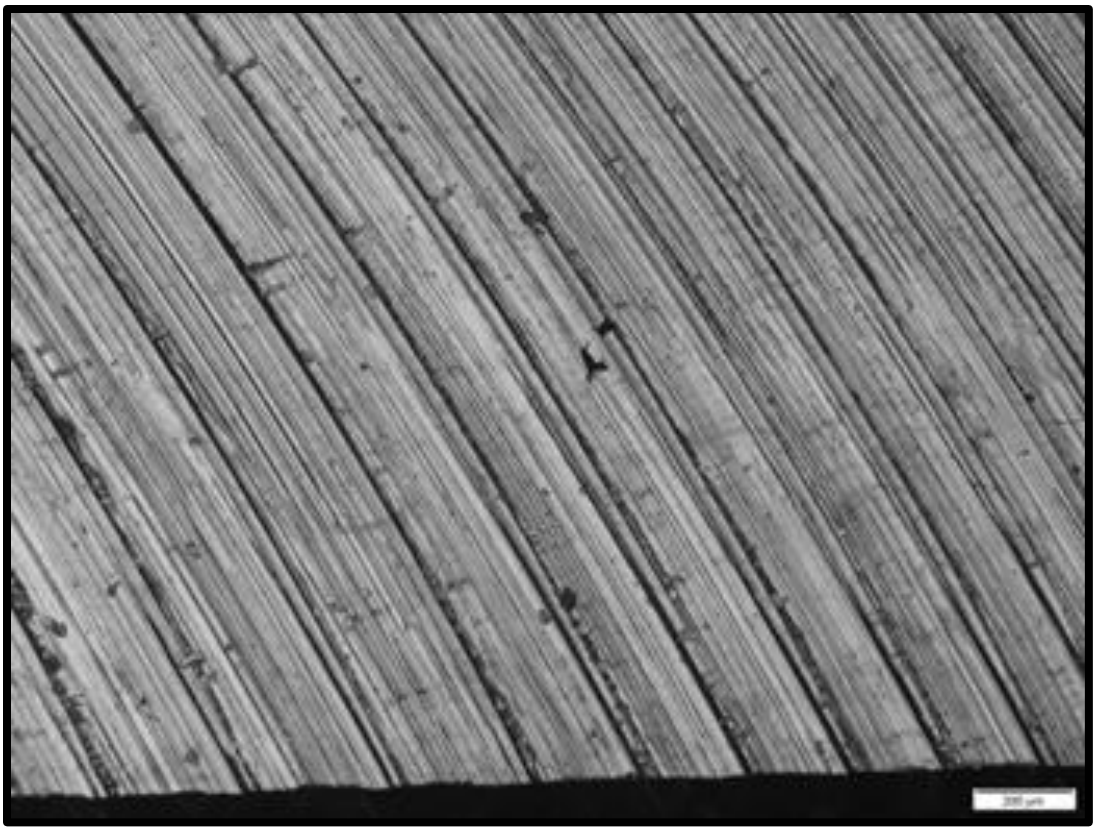

Figure 2.5 Milled specimen surface

The TAF specimens were also fabricated at UTEP in the W.M. Keck Center for 3D Innovation with a DECI Duo machine from PostProcess Technologies. This method of machining utilized a slurry made of alumina beads and water. The specimen would be held by a vise on a rotating platform and the pressurized slurry would be sprayed out of a nozzle that moved up and down the build direction of the specimen. Figure 2.6 outlines this method and the parameters used. Figure 2.7 depicts the surface of the TAF specimens.

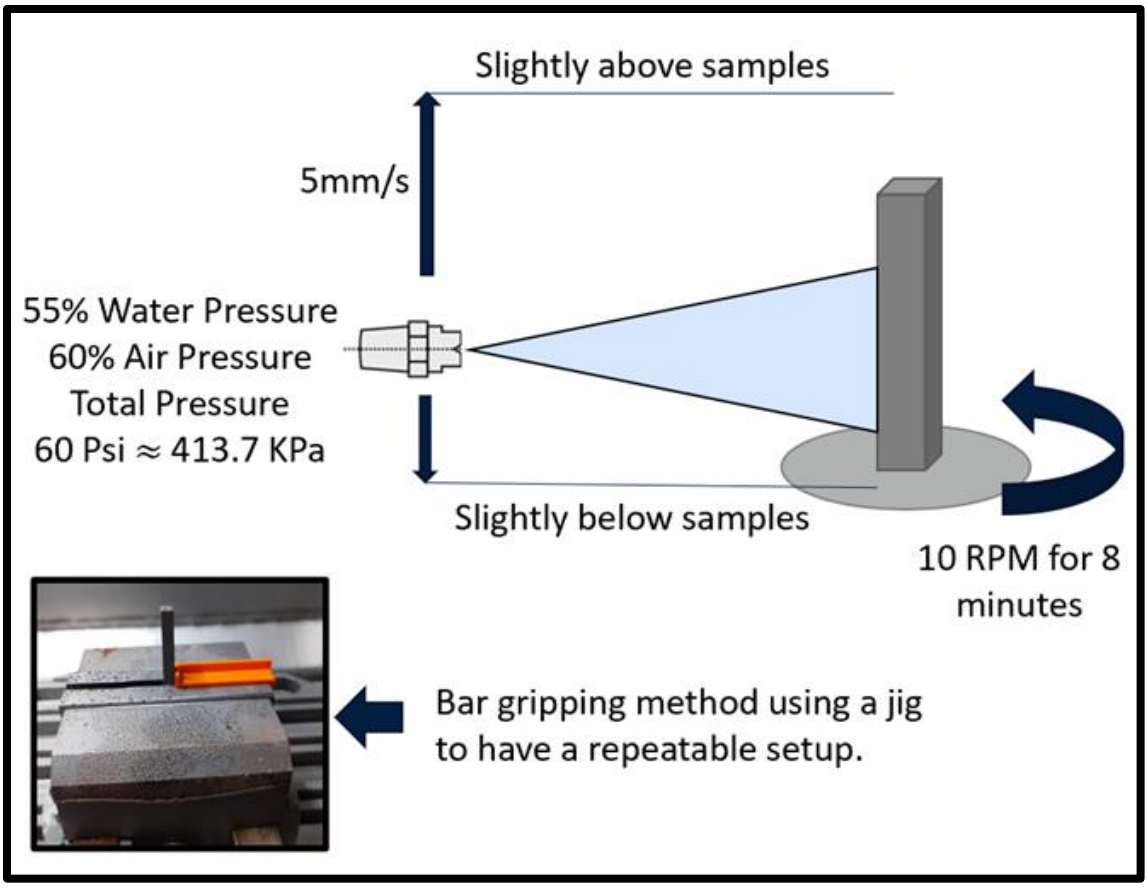

Figure 2.6 TAF surfacing parameters

Figure 2.7 TAF specimen surface

The surface ground specimens were machined by a third party. A grinding wheel was used to remove 0.5mm of material from each side of the rectangular bar. The wheel's rotation speed and accompanying parameters were not specified however, the grinding was done along the build direction with several passes until the desired depth was achieved. Figure 2.8 demonstrates how this method was applied. Figure 2.9 illustrates the surface of a surface ground specimen. Shallow scratches can be seen along the grinding direction.

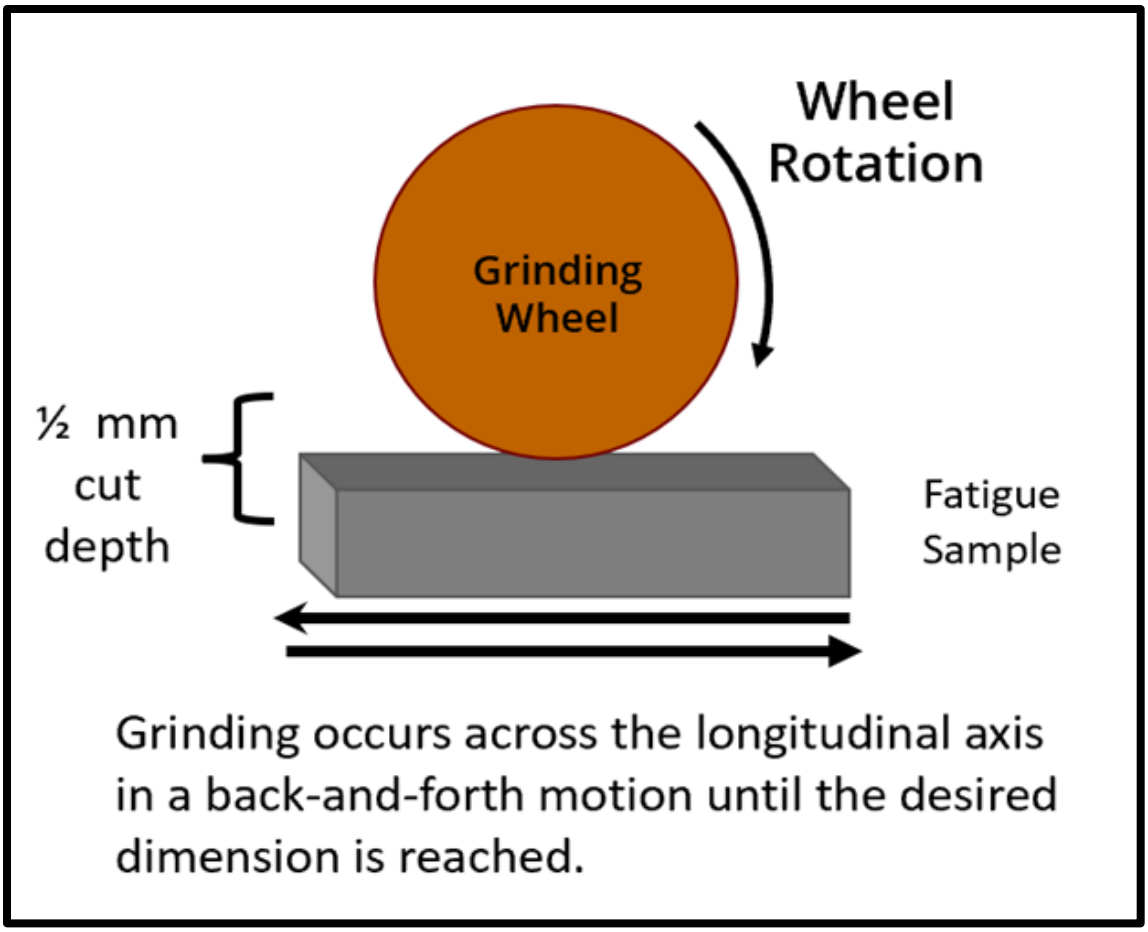

Figure 2.8 Grinding procedure

Figure 2.9 Surface ground specimen surface

Lastly, the remaining specimens were sent to Laboratory Testing Inc. (LTI) to be polished along the build direction. The parameters for this machining technique were not shared by the company, however they are industry certified to produce polished surfaces in compliance with aerospace and testing standards. They also guarantee a R_a value of less than 0.8 microns. Figure 2.10 illustrates the surface of a polished specimen. Shallow scratches can also be seen but unlike the ground sample's, the scratches more closely align with the build direction.

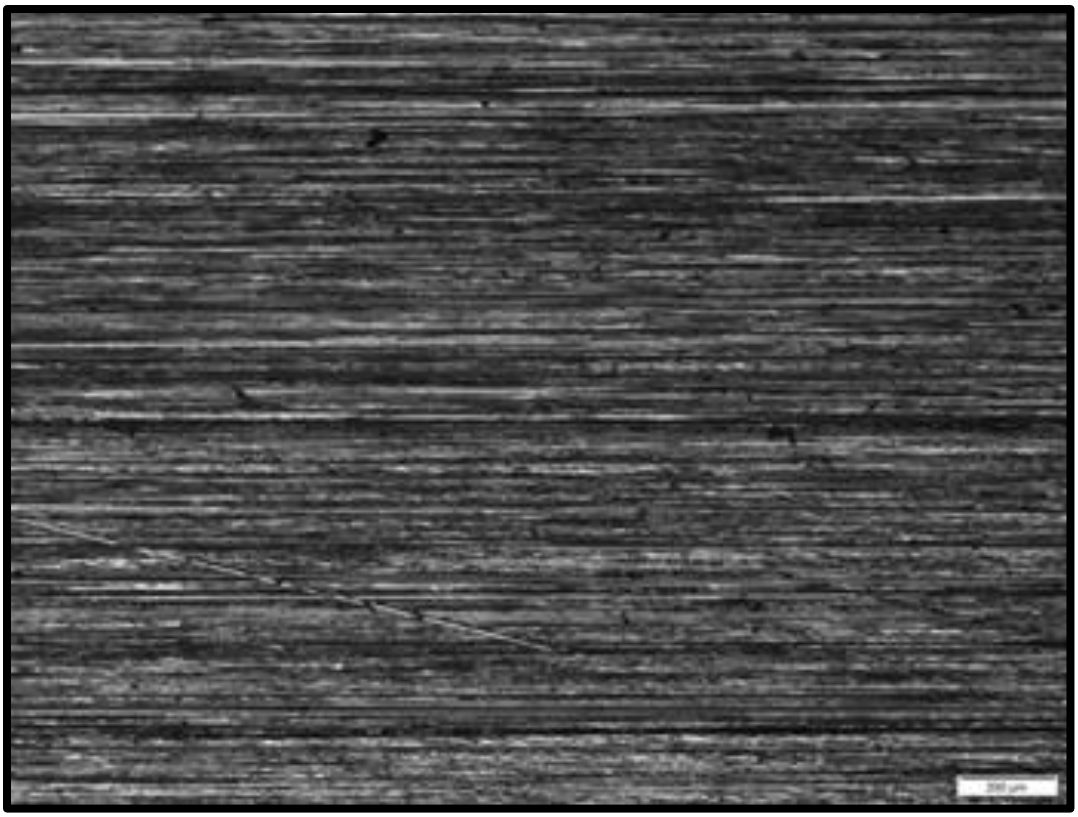

Figure 2.10 Polished specimen surface

2.4 Roughness Measurements

Contact and non-contact methods for measuring line roughness were used to analyze the top and bottom surfaces of the machined specimens. The contact method was done using a Mitutoyo Surftest SJ-210 mechanical profilometer. The non-contact method was done using a Keyence VR-5000 optical microscope. When analyzing the data for the non-contact method, the filters applied were the same used by the mechanical profilometer to make the measurements comparable. Figure 2.11 demonstrates how the specimens were analyzed on the VR-5000.

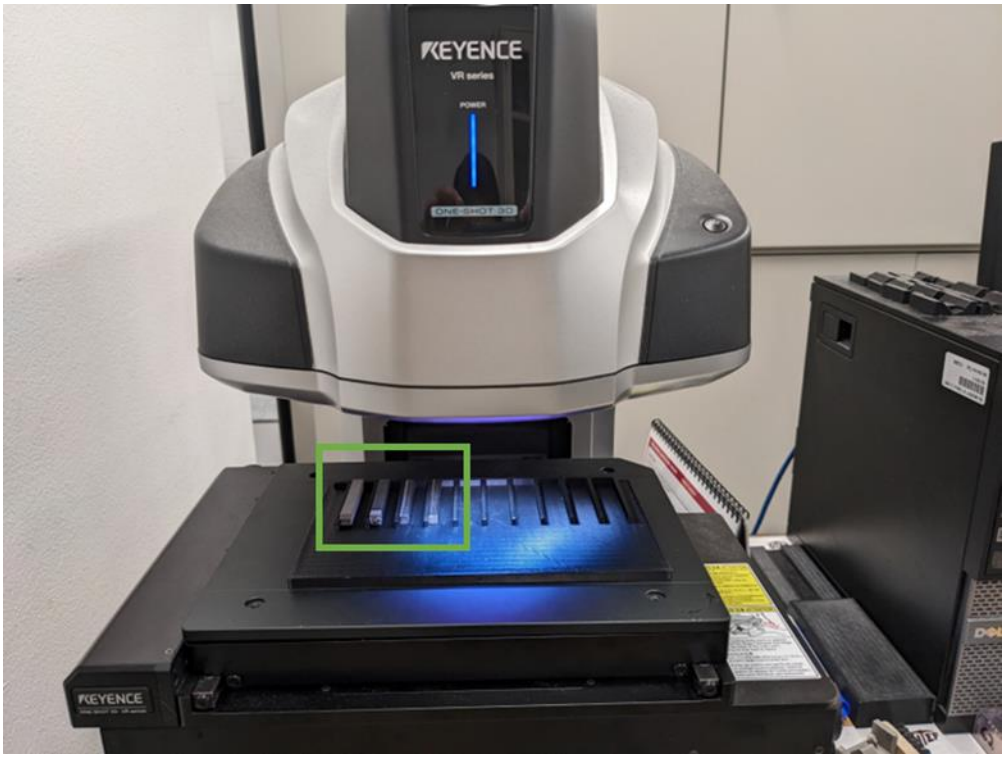

Figure 2.11 Scanning surface roughness via Keyence VR-5000

2.5 FATIGUE TESTING

The specimens were subject to four-point bending fatigue testing. The tests were performed on an MTS Landmark machine equipped with a 100 kilonewton (kN) load cell. The four-point test was a modified version where rather than gripping the rectangular bar, the specimen was held in place by four pins. The top pins were stationary and had a span of 10mm. The bottom pins were for loading and had a span of 30mm. Figure 2.12 illustrates the test setup. Because of the modified testing sequence, the stress ratio was 0.1; the stress ratio indicates the relationship between the maximum and minimum stress applied.

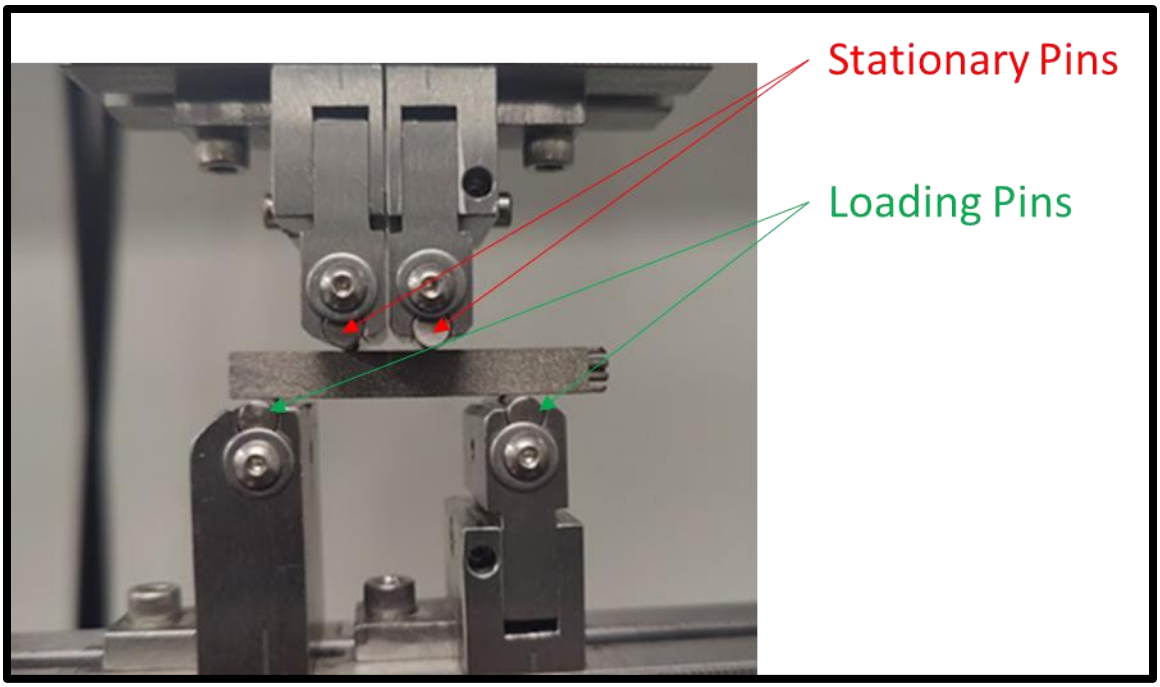

Figure 2.12 Fatigue test setup

Four maximum testing stresses were selected: 1200 MPa, 1067 MPa, 900 MPa, and 667 MPa. Three specimens from each machining technique were randomly allocated to each stress level. Table 2.2 illustration the test matrix for the experiment. The fatigue tests were conducted at a frequency of 10 hertz (Hz) until fracture. The machine would automatically stop the testing $7x10^6$ cycles; this was the cutoff point.

Table 2.2 Fatigue test matrix

Machining Method	1200 MPa	1067 MPa	900 MPa	667 MPa	Spares	Total
Milled	3	3	3	3	3	15
Thermal Atomized Fusillade (TAF)	3	3	3	3	3	15
Surface Ground	3	3	3	3	3	15
Polished	3	3	3	3	3	15
Total	12	12	12	12	12	60

2.6 FRACTURE SURFACE INSPECTION

The fracture surface of all the specimen that failed/broke during the fatigue testing were analyzed with a Keyence VHX optical microscope. The fracture surfaces were meticulously analyzed to identify the failure mechanism exhibited by the specimens, mainly the location of the fracture origin.

2.7 HARDNESS TESTING

Microhardness testing of the unloaded machined surfaces of all specimens was conducted using a QATM hardness tester. Microhardness tests are usually performed on the polished cross section of a specimen. However, the machined surfaces were analyzed in order to further understand the effects the machining techniques had on the specimens' mechanical properties.

Chapter 3: Results and Discussion

3.1 LINE ROUGHNESS

The line roughness values R_a and R_v of all specimens were categorized and analyzed according to the machining techniques. A high Ra and R_v indicates a worse surface quality, and a lower value indicates a better surface quality. Table 3.1 shows the average line roughness among the different post processes along with a comparison of the average line roughness of a sample with an as-built surface. Because previous studies demonstrated that R_v is more closely associated with fatigue life [44], this parameter was used to rank the machining techniques' quality in terms of expected fatigue performance. The ranking of best to worst surface finish is polished, surface ground, milled, and TAF, respectively. It should be noted that all machining techniques produced surfaces that were several magnitudes better than the as-built surface.

Table 3.1 Average line roughness per machining method

Machining Method	Average R_a (µm)	Average R_v (µm)
As-Built	22.51	48.17
Polished	0.164	.544
Surface Ground	0.440	1.737
Milled	1.101	3.167
TAF	1.041	4.112

In order to further understand the significance of the machining methods on the line roughness measurements, the R_v values were submitted to a one-way analysis of variance (ANOVA). The ANOVA was performed using Minitab, a statistical analysis software to compare the mean values with respect to each machining technique. In an ANOVA test, the null hypothesis is that the means do not differ, this indicates that there exists no difference among the parameters being compared. To reject the null hypothesis, a p-value of less than the acceptable error, in this and most cases 5 percent (0.05), must be produced from the ANOVA test. Figure 3.1 demonstrates the results from the ANOVA test. The p-value for this test was far below the acceptable error indicating that the means differ. In context, this constitutes that in terms of the line roughness R_v, the machining techniques are different from one another. However, this is only partially true. The polished and

surface ground sample are unique from one another, and all other machining methods explored as there is no overlap in the roughness measurements. The milled specimens expressed as 'Tangent Chamf' in figure 3.1 and TAF specimens (Deci Duo) are different from the polished and surface ground but not from each other. Due to the high variance in roughness values of the milled specimens, there is an overlap with the TAF specimens. Statistically, this means that there is no difference between the two machining techniques when compared by the line roughness R_v.

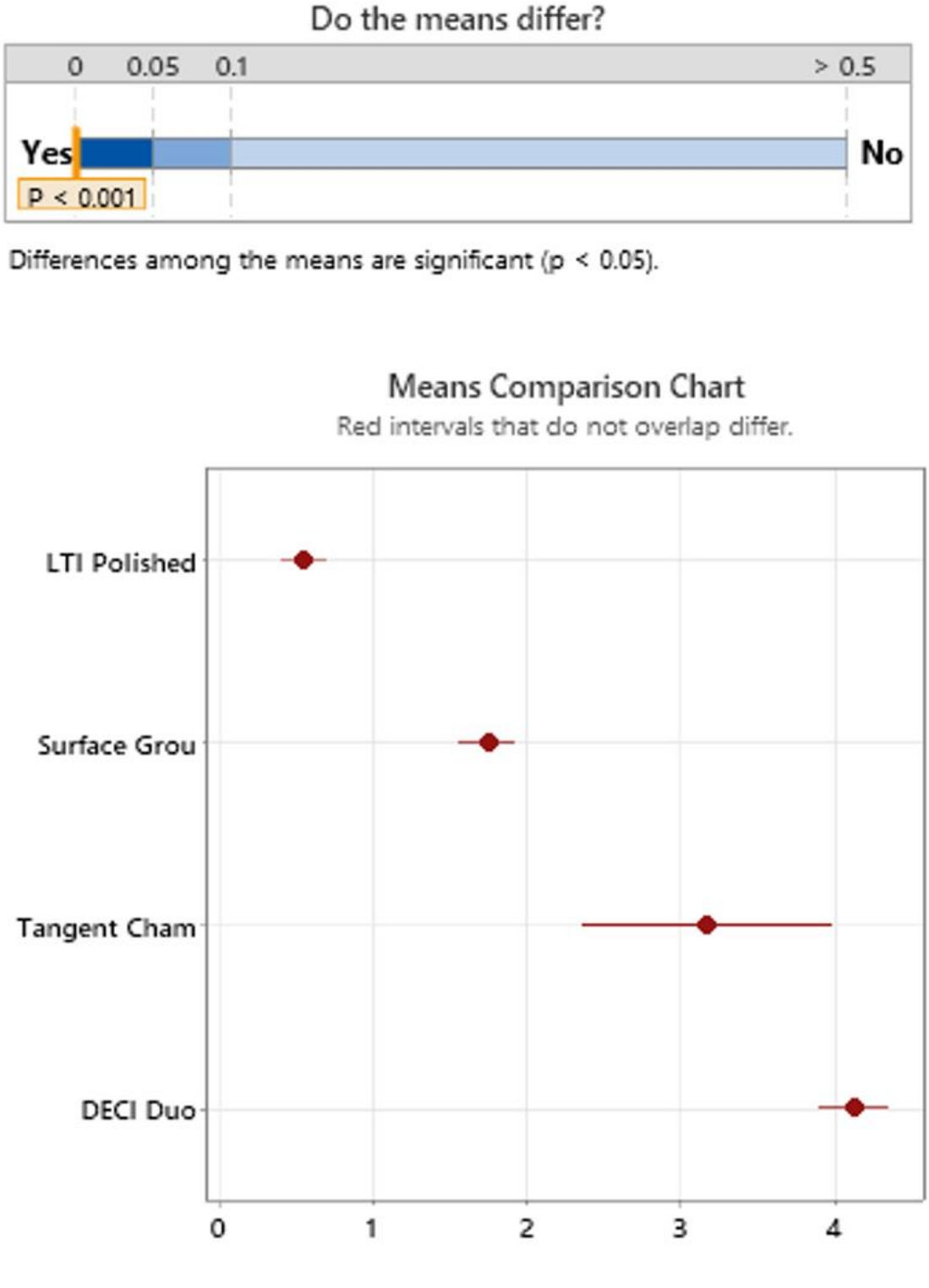

Figure 3.1 Line roughness (R_v) ANOVA results

3.2 FATIGUE RESULTS

The fatigue data was organized to compare the performance of the specimens with regards to their respective machining techniques. To facilitate the comparison, four different scatter plots were generated to compare the line roughness versus the cycles to failure at each of the four maximum testing stresses. Figures 3.2 to 3.5 depict the four plots with a best fit logarithmic line. The results from the two highest testing stresses are rather similar when compared to each other. Indeed, the trend of higher cycles to failure as the line roughness increases is apparent at both the maximum testing stress of 1200 MPa and 1067 MPa. The slopes of the lines of these two graphs also appeared to be very similar to one another. The similar trend continued when analyzing the performance at 900 MPa however, the slope of the line decreases significantly. Finally, the performance at 667 MPa seems to indicate and end to the trend as indicated by the flat line suggesting no correlation between the cycles to failure and the line roughness. Unfortunately, this flat line is due to the fact that at 667 MPa was the only testing stress where runoffs occurred, that is the fatigue test reached the $7x10^6$ cycle threshold and stopped. The presence of these runoff data points significantly skews the data to the right. The trend suggested by the plots contradicts the findings of Gockel et al. [44] that fatigue life improves when roughness decreases.

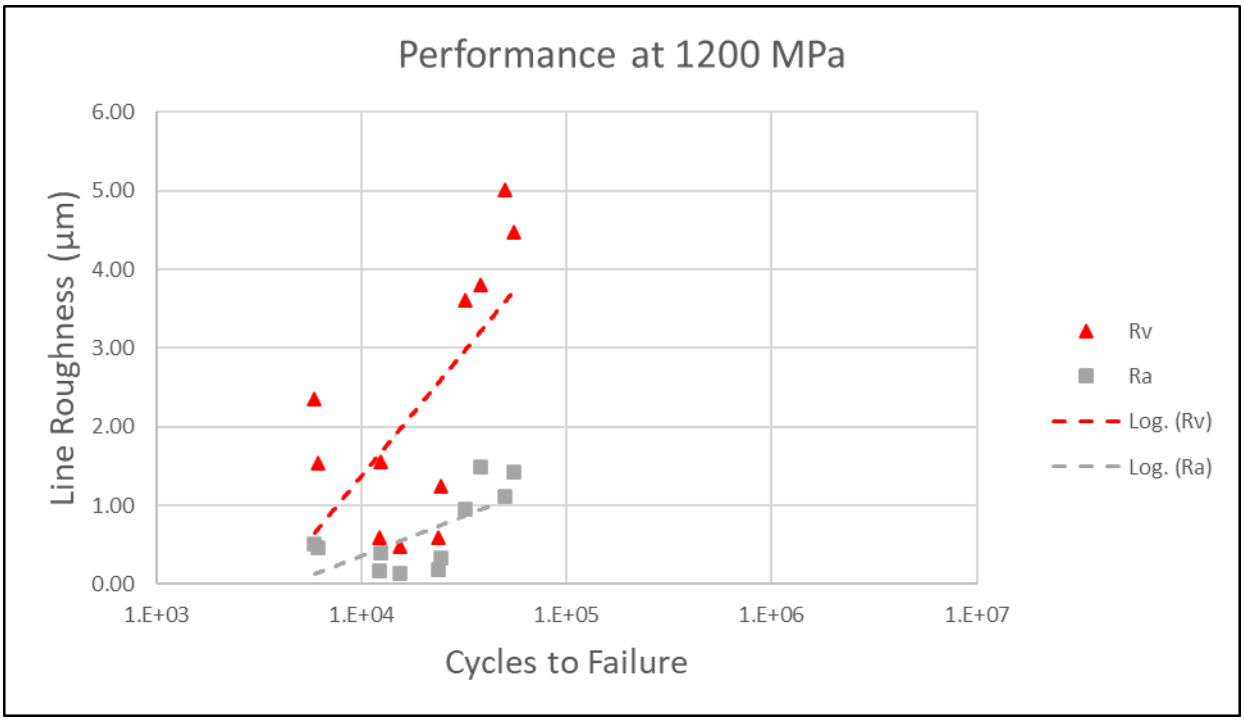

Figure 3.2 Line roughness vs. Cycles to failure at 1200 MPa

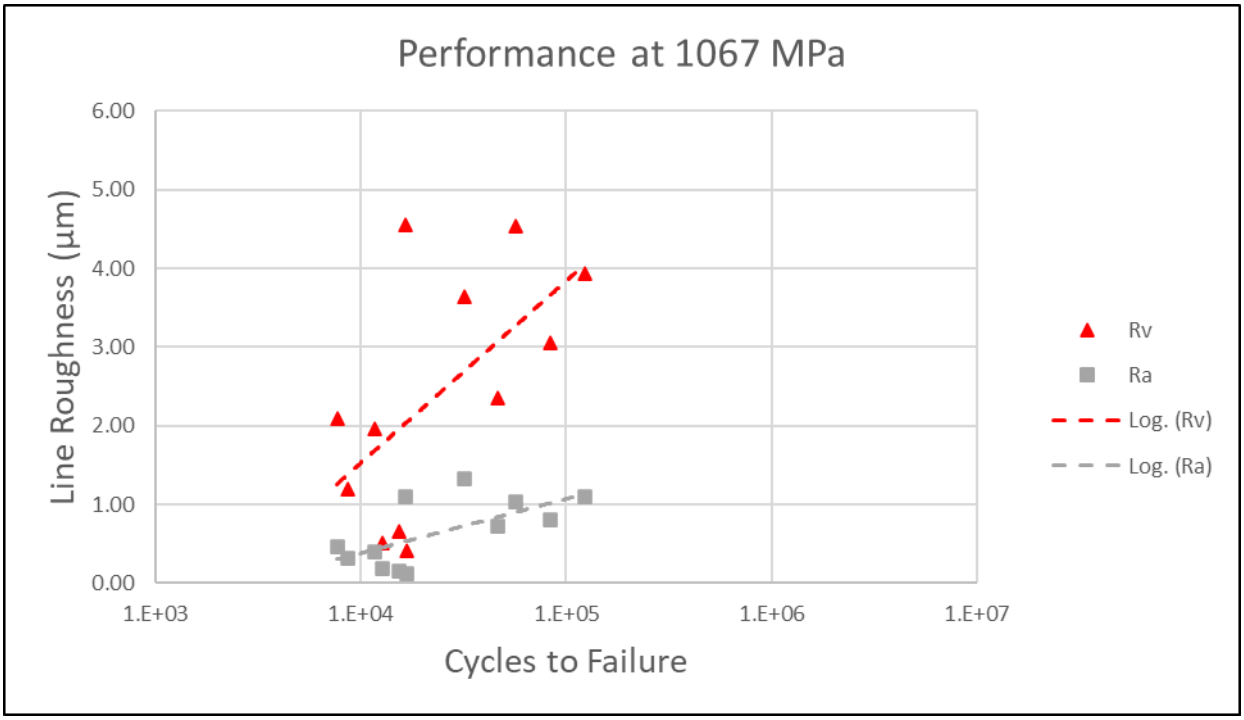

Figure 3.3 Line roughness vs. Cycles to failure at 1067 MPa

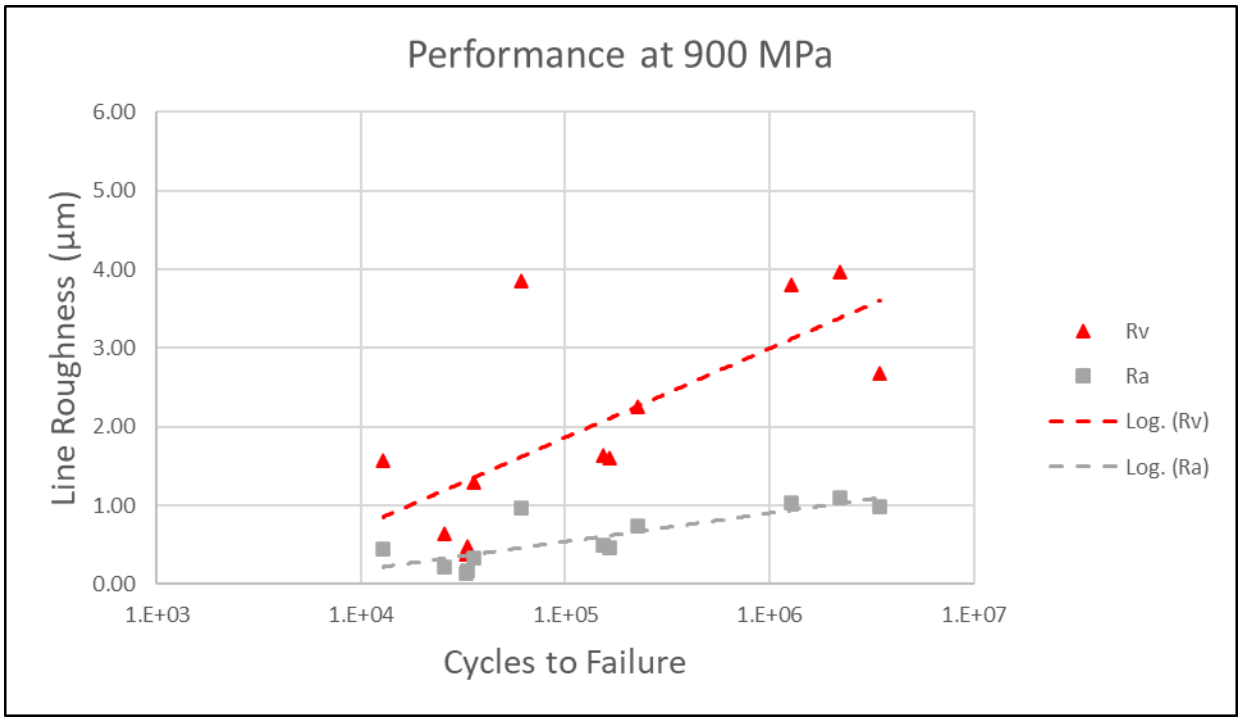

Figure 3.4 Line roughness vs. Cycles to failure at 900 MPa

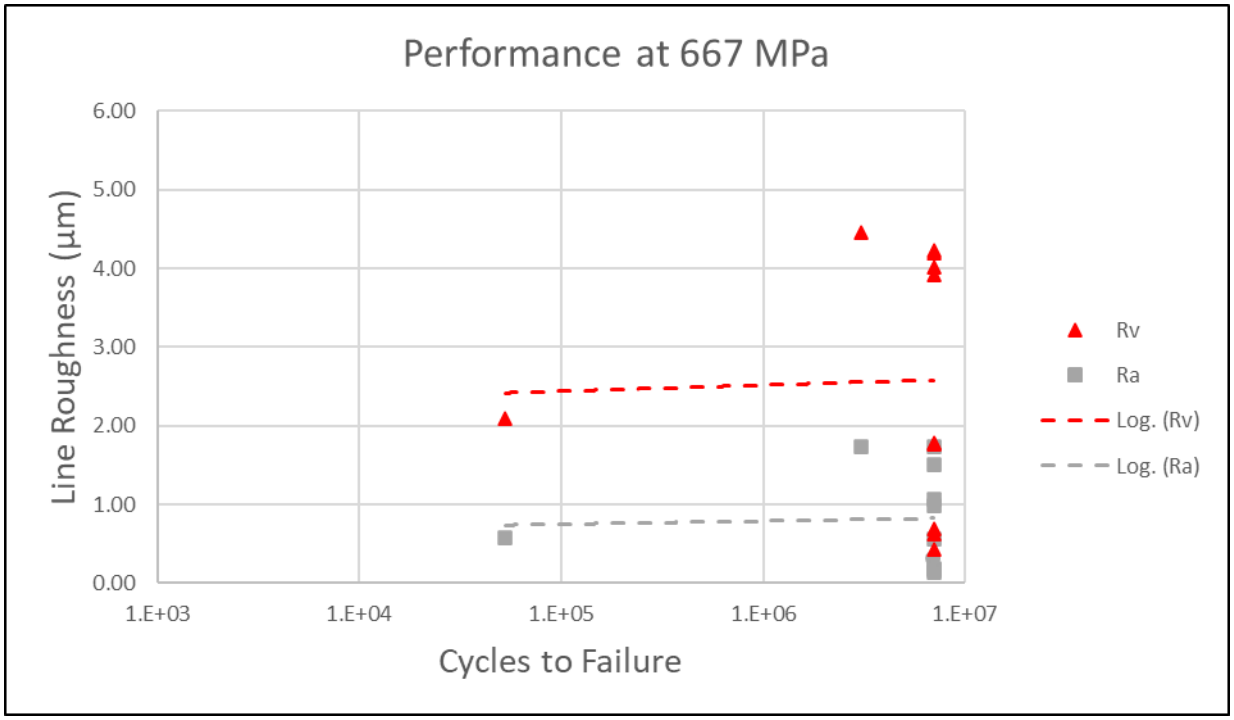

Figure 3.5 Line roughness vs. Cycles to failure at 667 MPa

Given that the previous plots suggested that a worse surface quality improved the fatigue life of the specimens, all the fatigue data was plotted to develop an S-N curve comparing the various machining techniques to another. To help better understand the significance of the machining, the data from a past study using as-built samples was included to further comprehend the effects of machining on the fatigue life. Because the as-built specimens were fatigue tested at lower stresses, the stress parameter was expressed as percentage of yield strength, so the data is comparable. Figure 3.6 depicts the S-N curve generated.

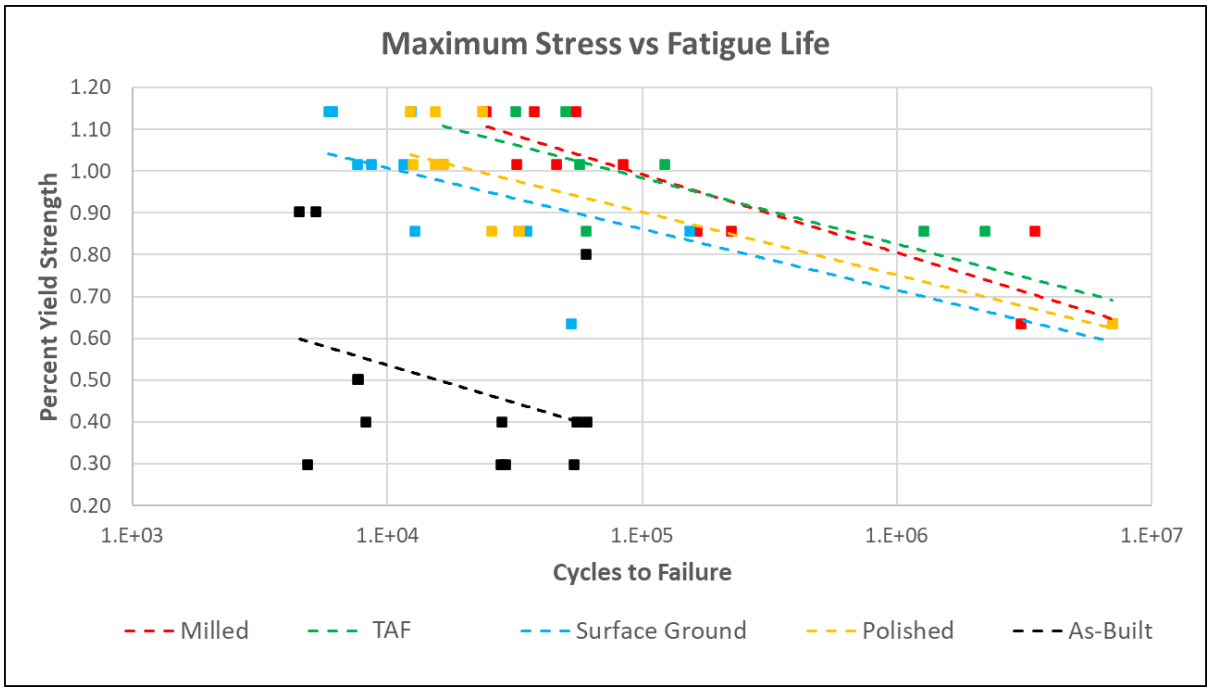

Figure 3.6 S-N curve comparing machining techniques

From the S-N curve, there is a significant improvement in the fatigue performance from as-built surfaces to the machined surfaces. This correlates with the notion that smoother surfaces have better fatigue endurance. However, the data between the machining methods indicates that the order of best performing technique to worst performing is TAF and milled, polished, and then surface ground. The fact that there is an overlap between the TAF and milled specimens on their fatigue performance reiterates the findings from the ANOVA which stated that there was no statistical difference between the two machining methods. However, the fact that these have the best performance of all the techniques despite having the worst surface quality is questionable.

To further understand if the machining techniques were truly affecting the fatigue life when compared to one another, a general linear model test was performed by using Minitab. The null hypothesis of this test is that there exists no significant correlation between the variables; the null hypothesis is rejected if the p-value is less than 0.05 as well. The variables that were compared were the cycles to failure versus the machining techniques and the stress levels. Figure 3.7 shows the results from the general linear model. Based on the p-values obtained, the machining methods do not seem to affect the fatigue life of the specimens, rather it is the testing stress that indicates an improvement and worsening of the fatigue performance. The latter statement makes sense, as the testing stress is lowered, it is expected that the specimen will endure more cycles until it reaches a point where it will infinitely run. This is the nature of all materials when subjected to stress. However, the idea that the machining does not affect fatigue life may be due to the fact that the roughness values are closely related to each other. It may be that at this scale, an improvement in the surface roughness is truly insignificant as far as the fatigue performance is concerned. However, the question remains why it appears that the specimens with worse surfaces outperformed the specimens with better surface quality.

Factor Information

Factor	Type	Levels	Values
Machining	Fixed	4	Milled, Polished, Surface Ground, TAF
Stress	Fixed	4	667, 900, 1067, 1200

Analysis of Variance

Source	DF	Adj SS	Adj MS	F-Value	P-Value
Machining	3	4.47934E+12	1.49311E+12	0.96	0.422
Stress	3	2.85075E+14	9.50252E+13	60.91	0.000

Figure 3.7 General linear model test results

3.3 FRACTURE SURFACE

Analysis of the fracture surface resulted in the identification of three locations for crack initiation. These are surface, chamfer, and defect. A surface initiation site refers to the fracture beginning on the bottom surface of the specimen. A chamfer initiation site refers to the fracture beginning on one of the chamfers near the bottom surface of the specimen. Lastly, a defect initiation indicates the fracture began at internal defect situated within the cross section of the specimen. A correlation between the fatigue life and the crack initiation site quickly became evident. Specimens with shortest to longest fatigue life were ordered from initiation sites of surface, chamfer, and then defect. The three initiation sites can be thought of as benchmarks whereas the number cyclical loadings increase, the failure site is surpassed one at a time until either the specimen fails at one of these or does not break and is labeled a runoff. Table 3.2 demonstrates the amount of each initiation

site across the machining techniques as well as the maximum and minimum cycles to failure at the specified site. It is important to note that only the milled and TAF specimens experienced crack initiation at an internal defect.

Table 3.2 Fracture initiation sites

Machining Technique	Initiation Site	Count	MAX Cycles	MIN Cycles
Milled	Surface	1	37,852	-
	Chamfer	5	84,112	24,496
	Defect	4	3,067,835	164,722
Surface Ground	Surface	9	52,885	5,883
	Chamfer	1	153,446	-
	Defect	0	-	-
TAF	Surface	5	122,415	16,535
	Chamfer	0	-	-
	Defect	4	2,216,812	60,430
Polished	Surface	4	16,648	12,313
	Chamfer	5	32,990	15,440
	Defect	0	-	-

While identifying the propagation (fatigue) and overload regions on the fracture surfaces, it was observed that the propagation regions grew in a similar fashion as the number of cycles to failures increased. Figures 3.8 to 3.10 illustrate this phenomenon with the propagation and overload regions highlighted in blue and red, respectively. Figure 3.8 depicts a TAF specimen with a surface fracture initiation site on the lower left side near the chamfer. Figure 3.9 depicts a polished specimen with a crack initiation site on the lower left side chamfer. Figure 3.10 depicts a TAF specimen with an initiation site at an internal defect.

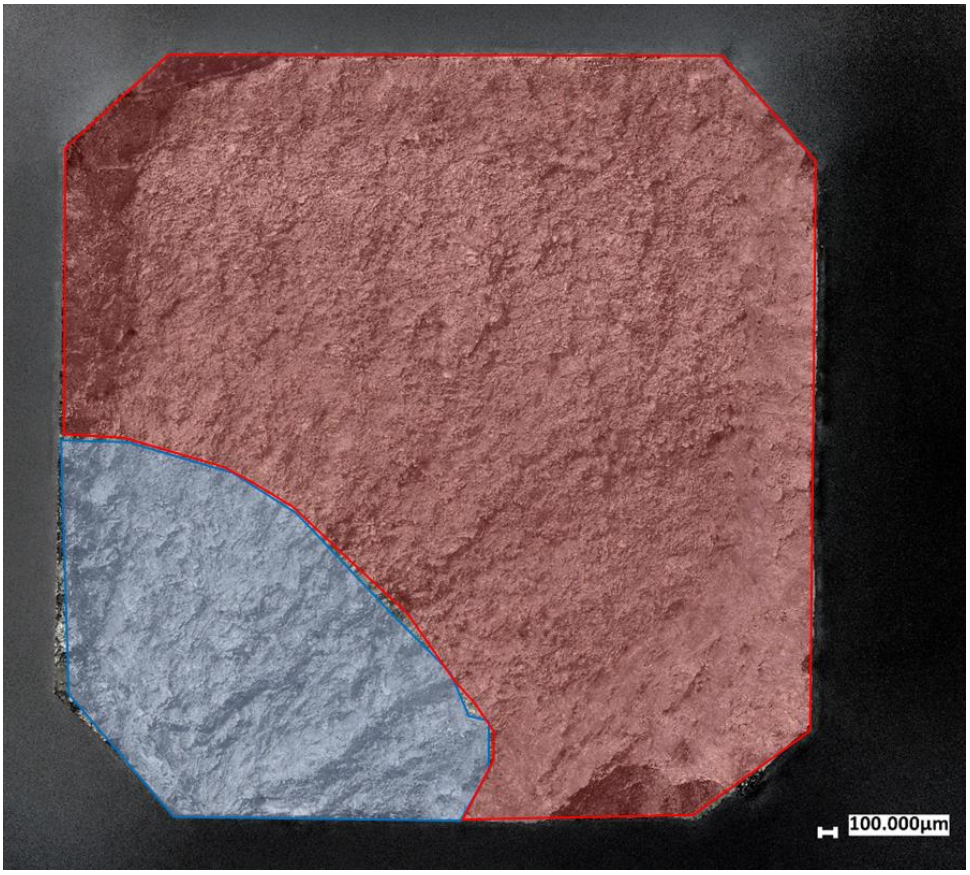

Figure 3.8 F17 (TAF) – Initiation site on the lower left surface near the chamfer

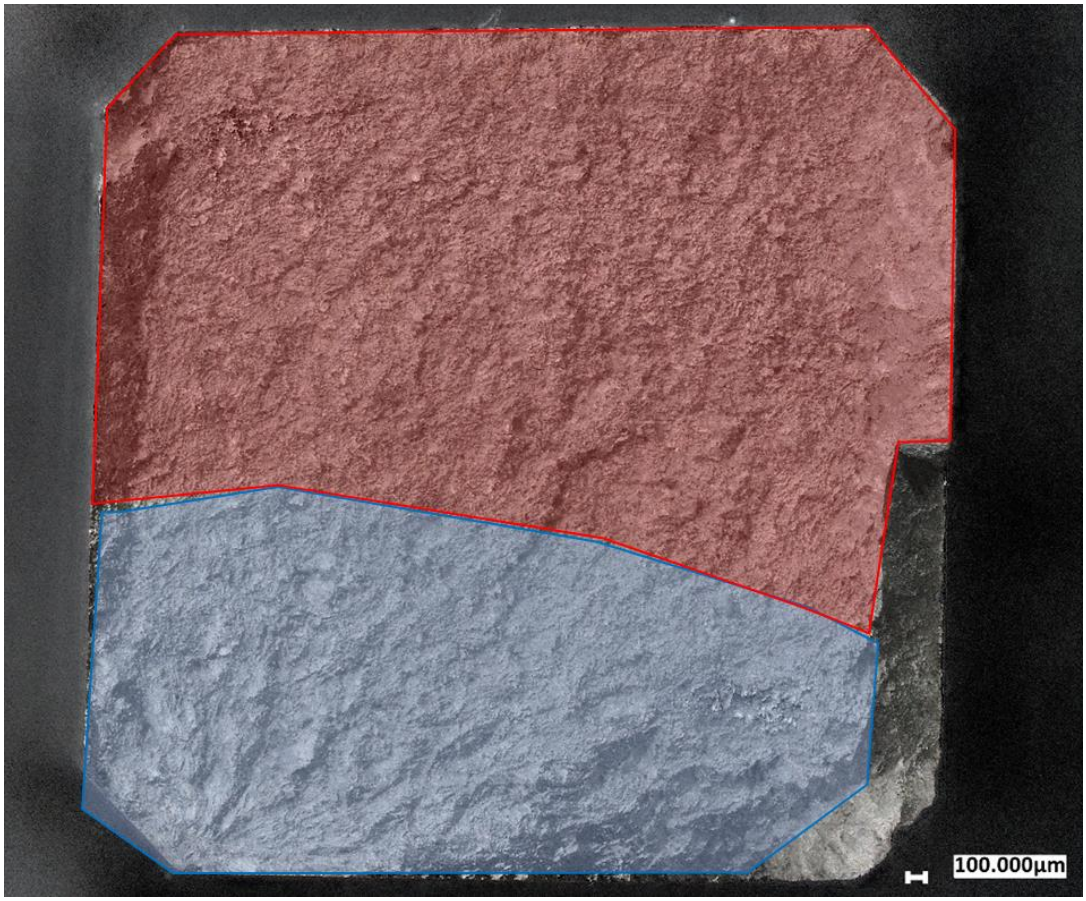

Figure 3.9 F49 (Polished)- Initiation site on the lower left side chamfer

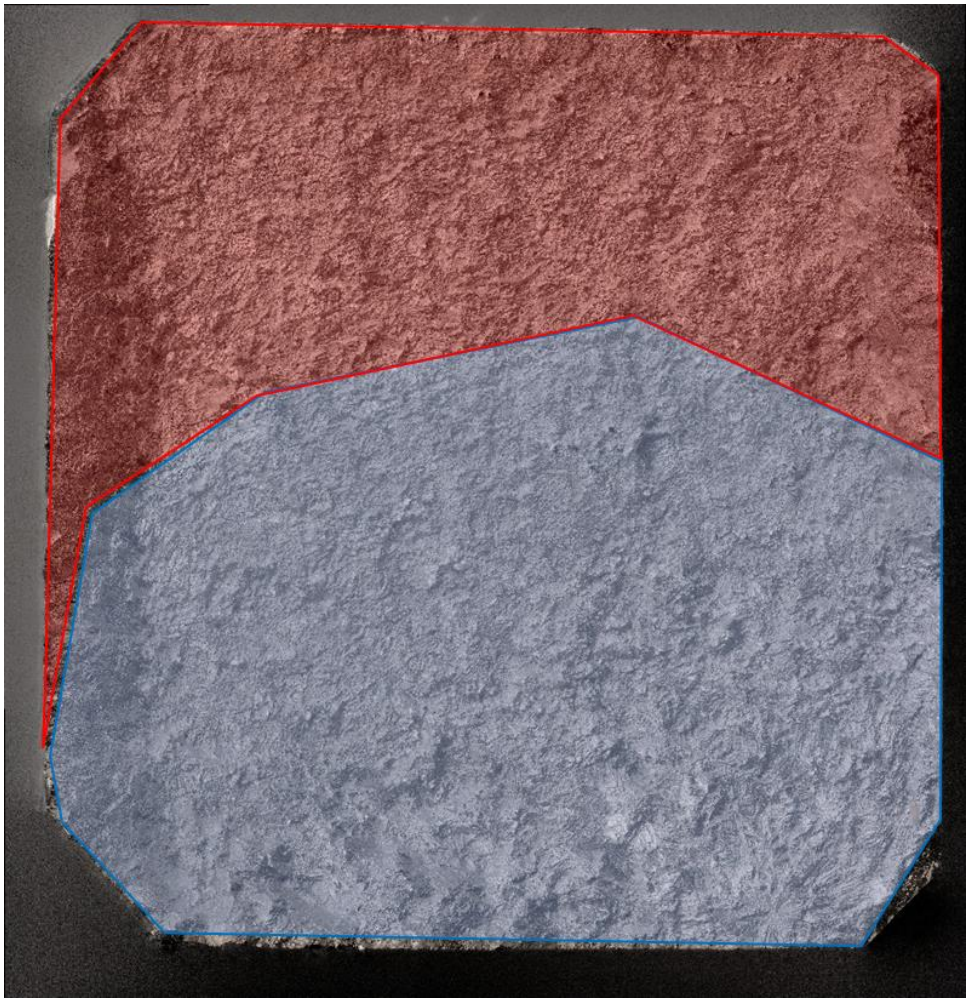

Figure 3.10 F77 (TAF)- Initiation site at defect on the lower right side

Further analysis of the specimens whose failure initiated at an internal defect demonstrated that internal defects where circular, possibly gas porosity, and were located near the bottom edge ranging from 100 microns at the nearest point and 500 microns at the furthest point. Figure 3.11 depicts a TAF specimen which failed at a defect of diameter of 29µm located 205µm from the bottom surface. Figure 3.12 depicts a milled specimen which failed at a defect of diameter of 27µm located 98µm from the bottom surface. Figure 3.13 depicts a TAF specimen which failed at a defect

of diameter of 35µm located 163µm from the bottom surface. Figure 3.14 depicts a TAF specimen which failed at a defect of diameter of 10µm located 284µm from the bottom surface. Figure 3.15 depicts a milled specimen which failed at a defect of diameter of 31µm located 511µm from the bottom surface. Figure 3.16 depicts a milled specimen which failed at a defect of diameter of 8µm located 203µm from the bottom surface. Figure 3.17 depicts a TAF specimen which failed at a defect of diameter of 8µm located 132µm from the bottom surface.

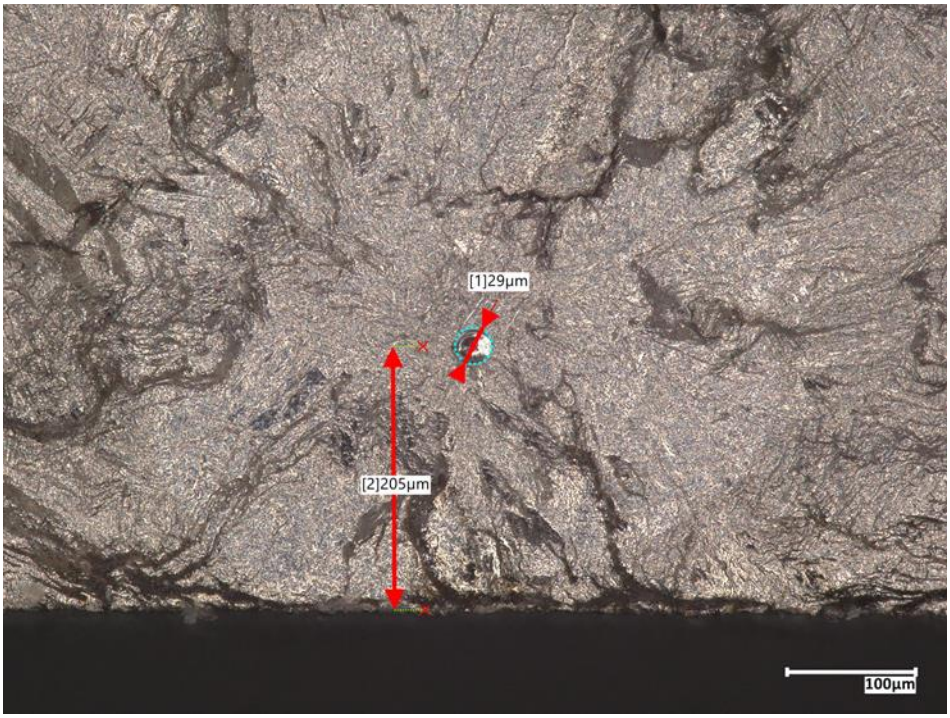

Figure 3.11 F30 (TAF)- Internal defect crack initiation

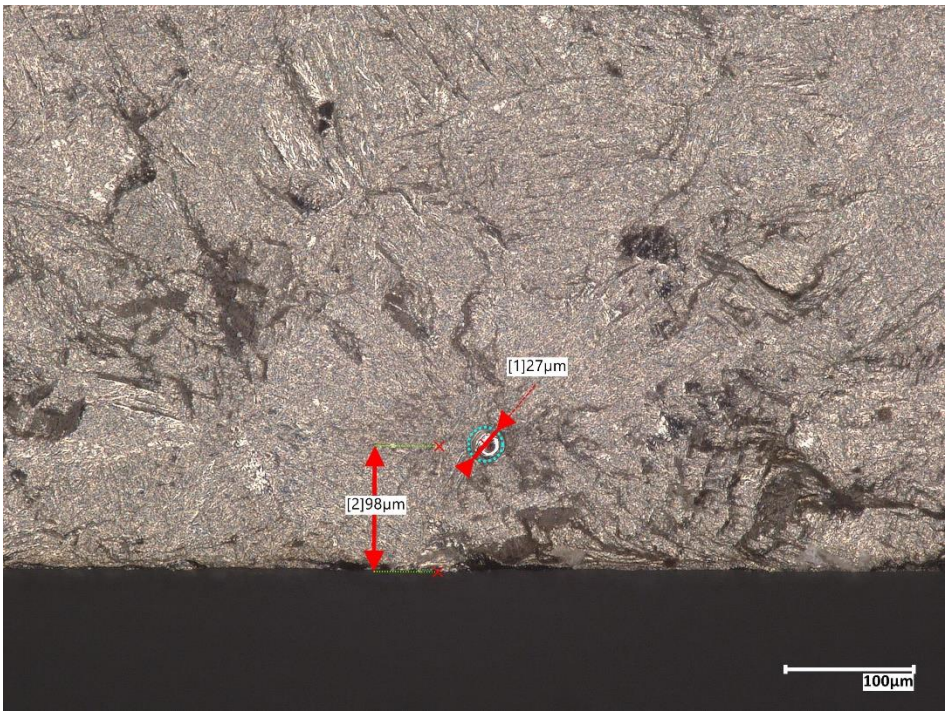

Figure 3.12 F34 (Milled)- Internal defect crack initiation

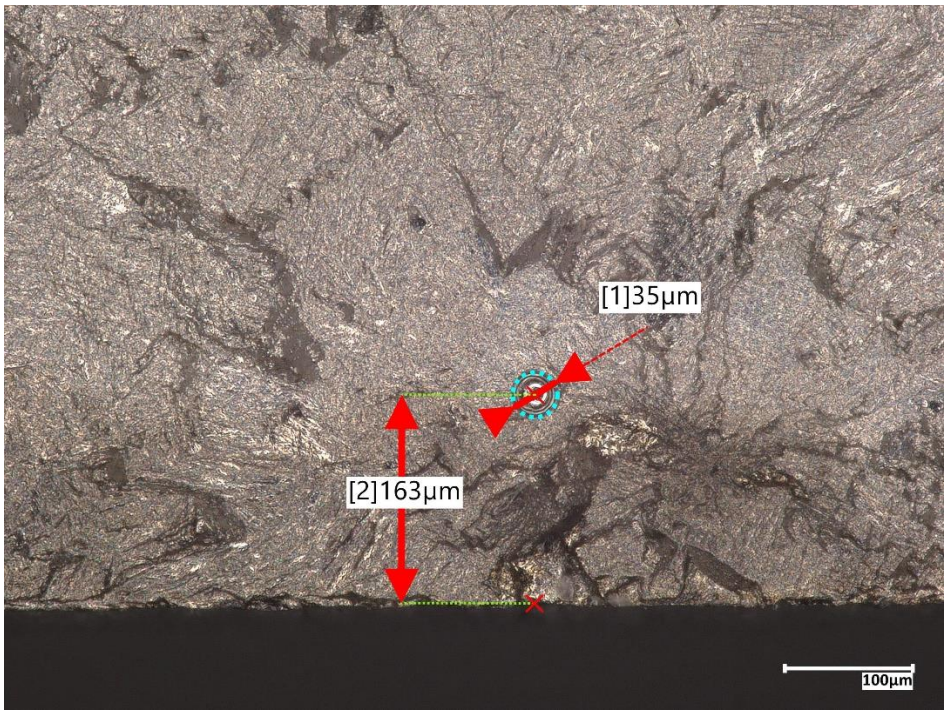

Figure 3.13 F82 (TAF)- Internal defect crack initiation

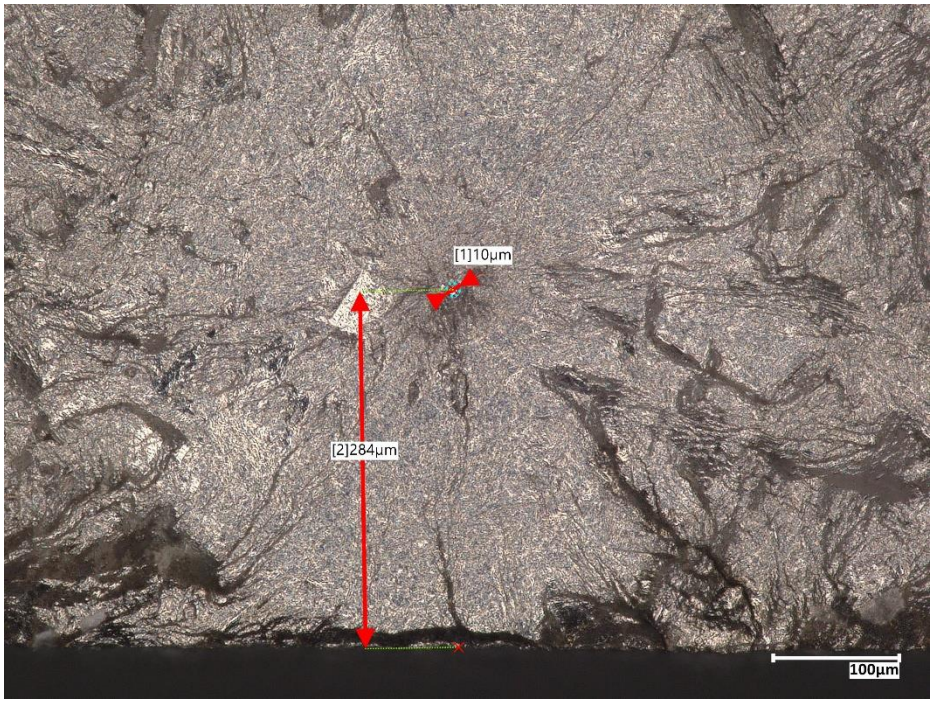

Figure 3.14 F47 (TAF)- Internal defect crack initiation

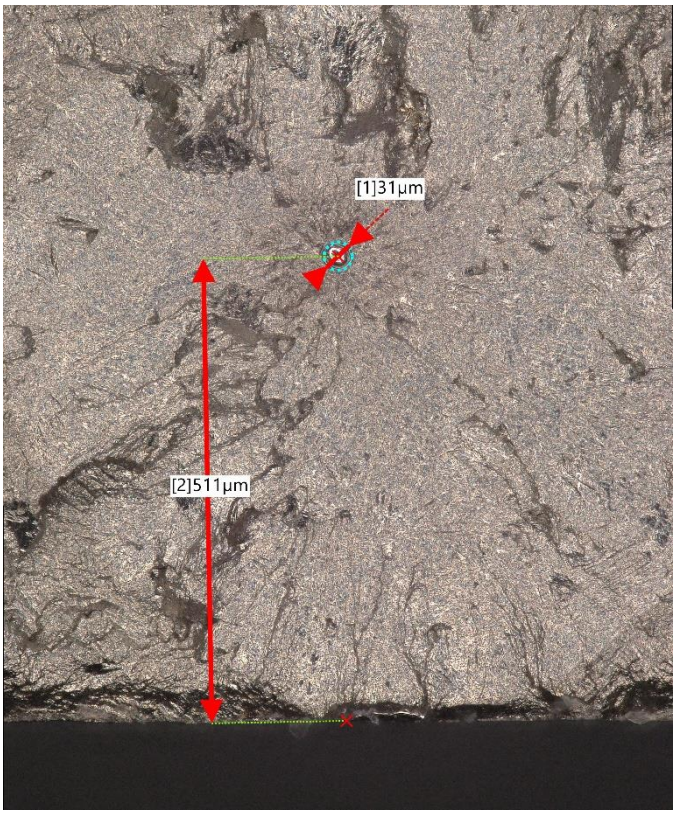

Figure 3.15 F61 (Milled)- Internal defect crack initiation

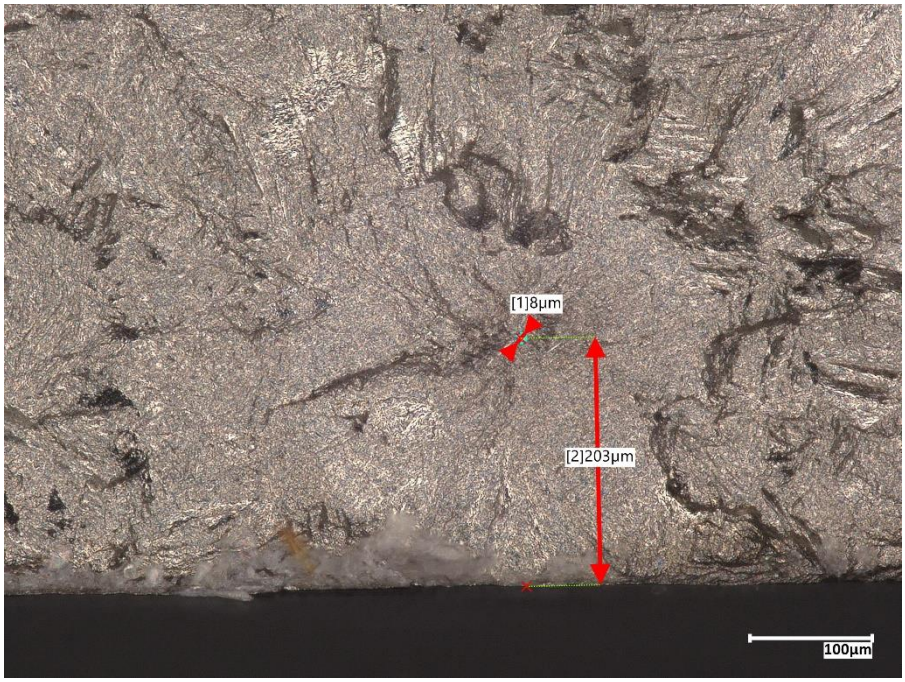

Figure 3.16 F77 (Milled)- Internal defect crack initiation

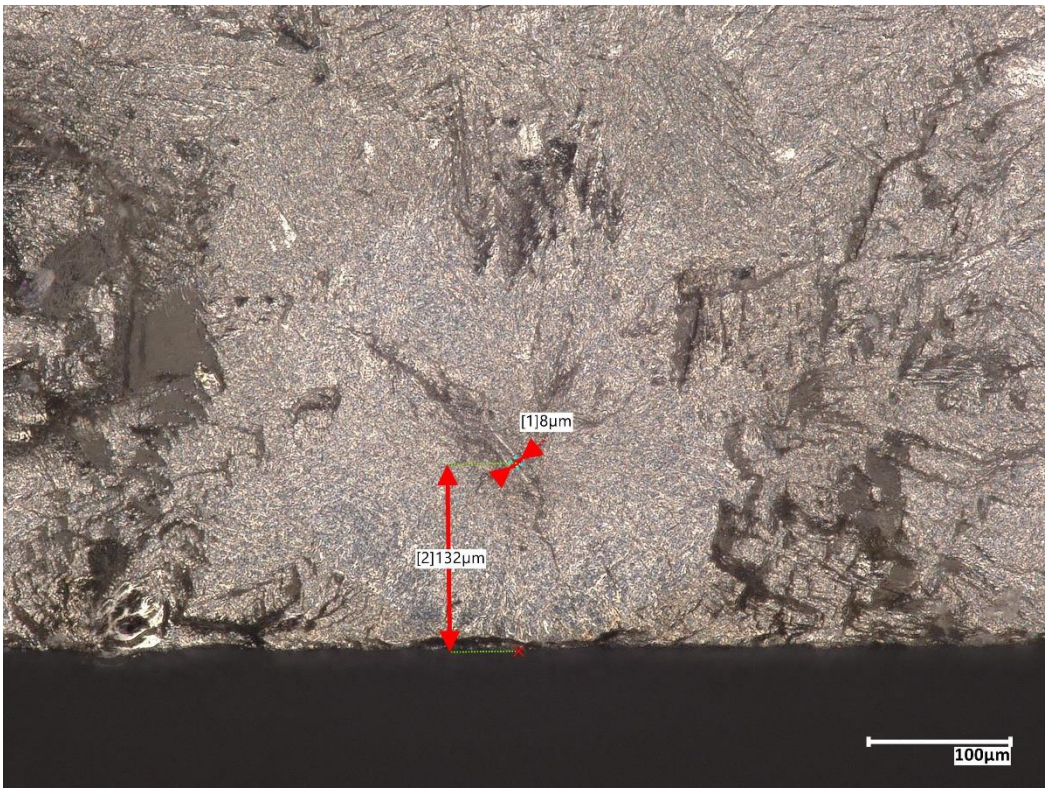

Figure 3.17 F78 (TAF)- Internal defect crack initiation

3.4 MICROHARDNESS

The microhardness data was analyzed on Minitab and an interval plot of hardness HV versus machining method was generated. Figure 3.18 demonstrates how the mean HV values compare between machining techniques. Overlapping occurs between the milled, polished, and surface ground specimens suggesting the difference in means is not statistically significant. The hardness values of the TAF specimens do not overlap with any of the other machining techniques suggesting that it is the only unique method in terms of microhardness. Despite this, the estimated hardness value means represented by the diamonds in figure 3.18 most closely resemble the fatigue performance of the corresponding machining techniques. It is reasonable then to propose that hardening of the material may have occurred during the different machining techniques, with TAF experiencing the most as evidenced by its larger hardness value. This work hardening event could lead to better fatigue performance.

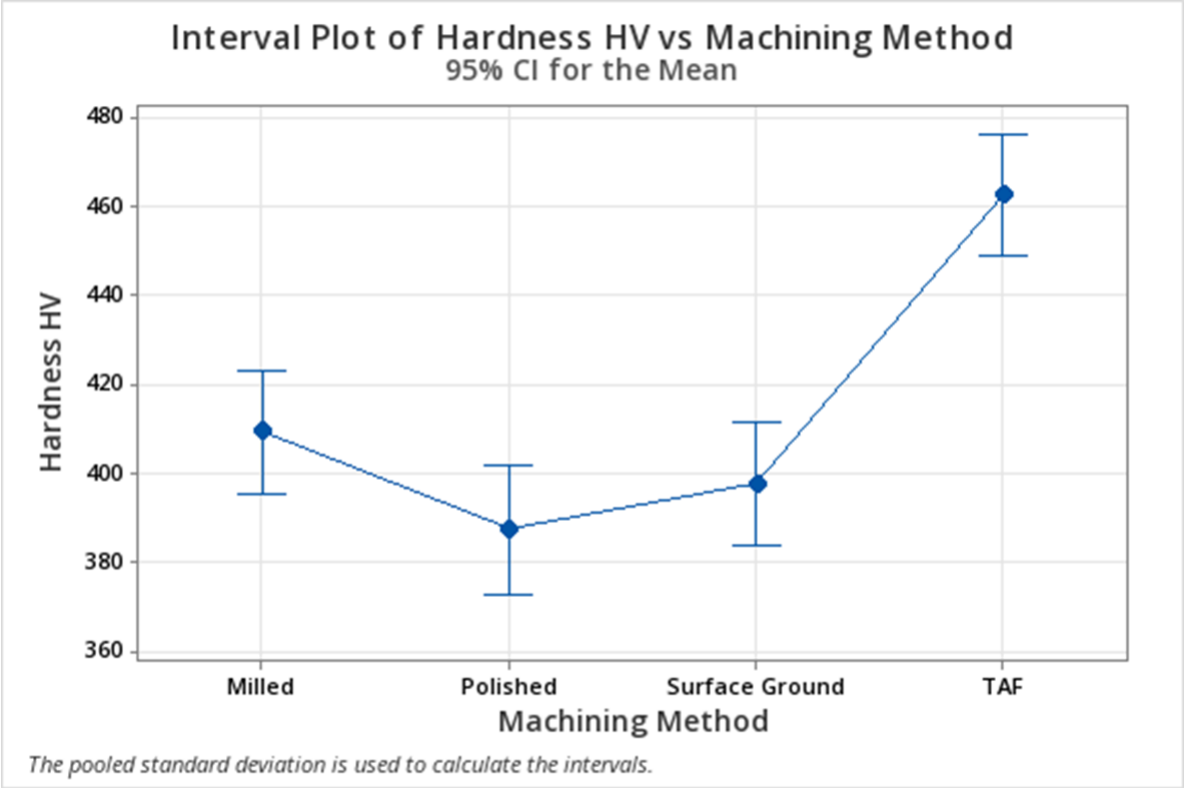

Figure 3.18 Hardness vs machining method interval plot

Chapter 4: Conclusions

Gockel et al. concluded that improving the surface quality of L-PBF parts leads to better fatigue performance [44]. This was shown to be true when analyzing the performance of as-built specimens versus machined specimens. The drastic improvement of the surface quality, or the drastic reduction in the line roughness R_v, had quite an immense impact on the fatigue life. This, however, was found to be true to only a certain extent.

Roughness of machined specimens with R_v of less than 6μm does not inversely correlate to fatigue endurance. Rather, the opposite relationship was observed at high stress levels. Furthermore, machining of the specimens appeared to have work hardened the surfaces of the specimens. Work hardening is known to improve the mechanical properties of materials such as fatigue endurance.

References

[1] E. Giacosa, E. Crocco, J. Kubálek, and F. Culasso, “Additive manufacturing in international business: Bridging academic and practitioners’ perspectives,” *J. Int. Manag.*, p. 101151, Apr. 2024, doi: 10.1016/j.intman.2024.101151.

[2] R. Mastrullo, A. W. Mauro, F. Pelella, and L. Viscito, “Process control and energy saving in the ladle stage of a metal casting process through physics-based and ANN-based modelling approaches,” *Appl. Therm. Eng.*, vol. 248, p. 123135, Jul. 2024, doi: 10.1016/j.applthermaleng.2024.123135.

[3] P. Beeley, “Introduction,” in *Foundry Technology (Second Edition)*, P. Beeley, Ed., Oxford: Butterworth-Heinemann, 2001, pp. 1–14. doi: 10.1016/B978-075064567-6/50003-0.

[4] H. Luo, Y. Zhang, J. Yu, X. Dong, and T. Zhou, “Additive, subtractive and formative manufacturing of glass-based functional micro/nanostructures: A comprehensive review,” *Mater. Des.*, vol. 233, p. 112285, Sep. 2023, doi: 10.1016/j.matdes.2023.112285.

[5] G. A. Abureden, W. M. Hasan, and A. N. Ababneh, “Exploring potential benefits of additive manufacturing in creating corrugated web steel beams,” *J. Constr. Steel Res.*, vol. 187, p. 106975, Dec. 2021, doi: 10.1016/j.jcsr.2021.106975.

[6] T. D. Ngo, A. Kashani, G. Imbalzano, K. T. Q. Nguyen, and D. Hui, “Additive manufacturing (3D printing): A review of materials, methods, applications and challenges,” *Compos. Part B Eng.*, vol. 143, pp. 172–196, Jun. 2018, doi: 10.1016/j.compositesb.2018.02.012.

[7] F42 Committee, “Terminology for Additive Manufacturing Technologies,.” ASTM International. doi: 10.1520/F2792-12A.

[8] S. Chowdhury *et al.*, “Laser powder bed fusion: a state-of-the-art review of the technology, materials, properties & defects, and numerical modelling,” *J. Mater. Res. Technol.*, vol. 20, pp. 2109–2172, Sep. 2022, doi: 10.1016/j.jmrt.2022.07.121.

[9] Y. Song, Y. Ghafari, A. Asefnejad, and D. Toghraie, “An overview of selective laser sintering 3D printing technology for biomedical and sports device applications: Processes, materials, and applications,” *Opt. Laser Technol.*, vol. 171, p. 110459, Apr. 2024, doi: 10.1016/j.optlastec.2023.110459.

[10] G. Hussain *et al.*, “Design and development of a lightweight SLS 3D printer with a controlled heating mechanism: Part A,” *Int. J. Lightweight Mater. Manuf.*, vol. 2, no. 4, pp. 373–378, Dec. 2019, doi: 10.1016/j.ijlmm.2019.01.005.

[11] S. Thiede, M. Wiese, and C. Herrmann, “Upscaling strategies for polymer additive manufacturing: an assessment from economic and environmental

perspective for SLS, MJF and DLP," *Procedia CIRP*, vol. 104, pp. 653–658, Jan. 2021, doi: 10.1016/j.procir.2021.11.110.

[12] D. Gu, *Laser Additive Manufacturing of High-Performance Materials*. Springer, 2015.

[13] D. Gu and Y. Shen, "Balling phenomena in direct laser sintering of stainless steel powder: Metallurgical mechanisms and control methods," *Mater. Des.*, vol. 30, no. 8, pp. 2903–2910, Sep. 2009, doi: 10.1016/j.matdes.2009.01.013.

[14] H. J. Niu and I. T. H. Chang, "Instability of scan tracks of selective laser sintering of high speed steel powder," *Scr. Mater.*, vol. 41, no. 11, pp. 1229–1234, Nov. 1999, doi: 10.1016/S1359-6462(99)00276-6.

[15] H. J. Niu and I. T. H. Chang, "Selective laser sintering of gas and water atomized high speed steel powders," *Scr. Mater.*, vol. 41, no. 1, pp. 25–30, Jun. 1999, doi: 10.1016/S1359-6462(99)00089-5.

[16] H. J. Niu and I. T. H. Chang, "Liquid phase sintering of M3/2 high speed steel by selective laser sintering," *Scr. Mater.*, vol. 39, no. 1, pp. 67–72, Jun. 1998, doi: 10.1016/S1359-6462(98)00126-2.

[17] A. N. Chatterjee, S. Kumar, P. Saha, P. K. Mishra, and A. R. Choudhury, "An experimental design approach to selective laser sintering of low carbon steel," *J. Mater. Process. Technol.*, vol. 136, no. 1, pp. 151–157, May 2003, doi: 10.1016/S0924-0136(03)00132-8.

[18] K. Murali *et al.*, “Direct selective laser sintering of iron–graphite powder mixture,” *J. Mater. Process. Technol.*, vol. 136, no. 1, pp. 179–185, May 2003, doi: 10.1016/S0924-0136(03)00150-X.

[19] D. Gu *et al.*, “Densification behavior, microstructure evolution, and wear performance of selective laser melting processed commercially pure titanium,” *Acta Mater.*, vol. 60, no. 9, pp. 3849–3860, May 2012, doi: 10.1016/j.actamat.2012.04.006.

[20] Q. Jia and D. Gu, “Selective laser melting additive manufacturing of Inconel 718 superalloy parts: Densification, microstructure and properties,” *J. Alloys Compd.*, vol. 585, pp. 713–721, Feb. 2014, doi: 10.1016/j.jallcom.2013.09.171.

[21] D. Dai and D. Gu, “Thermal behavior and densification mechanism during selective laser melting of copper matrix composites: Simulation and experiments,” *Mater. Des.*, vol. 55, pp. 482–491, Mar. 2014, doi: 10.1016/j.matdes.2013.10.006.

[22] Y. Wang, J. Bergström, and C. Burman, “Characterization of an iron-based laser sintered material,” *J. Mater. Process. Technol.*, vol. 172, no. 1, pp. 77–87, Feb. 2006, doi: 10.1016/j.jmatprotec.2005.09.004.

[23] M. Xia, D. Gu, G. Yu, D. Dai, H. Chen, and Q. Shi, “Porosity evolution and its thermodynamic mechanism of randomly packed powder-bed during

selective laser melting of Inconel 718 alloy," *Int. J. Mach. Tools Manuf.*, vol. 116, pp. 96–106, May 2017, doi: 10.1016/j.ijmachtools.2017.01.005.

[24] K. Monroy, J. Delgado, and J. Ciurana, "Study of the Pore Formation on CoCrMo Alloys by Selective Laser Melting Manufacturing Process," *Procedia Eng.*, vol. 63, pp. 361–369, Jan. 2013, doi: 10.1016/j.proeng.2013.08.227.

[25] "Figure 7. Gas porosity and lack of fusion defects during SLM of A)...," ResearchGate. Accessed: Apr. 28, 2024. [Online]. Available: https://www.researchgate.net/figure/Gas-porosity-and-lack-of-fusion-defects-during-SLM-of-A-hybrid-powder-and-B-reference_fig5_344674182

[26] Weiheng, "Shrinkage Porosity Solution During Aluminum Die Casting," Weiheng. Accessed: Apr. 28, 2024. [Online]. Available: https://www.prodiecasting.com/how-to-solve-shrinkage-porosity/

[27] R. Xiao and X. Zhang, "Problems and issues in laser beam welding of aluminum–lithium alloys," *J. Manuf. Process.*, vol. 16, no. 2, pp. 166–175, Apr. 2014, doi: 10.1016/j.jmapro.2013.10.005.

[28] Y. Li, H. Yang, X. Lin, W. Huang, J. Li, and Y. Zhou, "The influences of processing parameters on forming characterizations during laser rapid forming," *Mater. Sci. Eng. A*, vol. 360, no. 1, pp. 18–25, Nov. 2003, doi: 10.1016/S0921-5093(03)00435-0.

[29] S. L. Sing, J. An, W. Y. Yeong, and F. E. Wiria, “Laser and electron-beam powder-bed additive manufacturing of metallic implants: A review on processes, materials and designs,” *J. Orthop. Res.*, vol. 34, no. 3, pp. 369–385, 2016, doi: 10.1002/jor.23075.

[30] C. M. Chen and R. Kovacevic, “Finite element modeling of friction stir welding—thermal and thermomechanical analysis,” *Int. J. Mach. Tools Manuf.*, vol. 43, no. 13, pp. 1319–1326, Oct. 2003, doi: 10.1016/S0890-6955(03)00158-5.

[31] “Library,” *MRS Bull.*, vol. 28, no. 9, pp. 674–675, Sep. 2003, doi: 10.1557/mrs2003.197.

[32] M. Shiomi, K. Osakada, K. Nakamura, T. Yamashita, and F. Abe, “Residual Stress within Metallic Model Made by Selective Laser Melting Process,” *CIRP Ann.*, vol. 53, no. 1, pp. 195–198, Jan. 2004, doi: 10.1016/S0007-8506(07)60677-5.

[33] C. Y. Poon and B. Bhushan, “Comparison of surface roughness measurements by stylus profiler, AFM and non-contact optical profiler,” *Wear*, vol. 190, no. 1, pp. 76–88, Nov. 1995, doi: 10.1016/0043-1648(95)06697-7.

[34] V. Lyukshin, D. Shatko, and P. Strelnikov, “Methods and approaches to the surface roughness assessment,” *Mater. Today Proc.*, vol. 38, pp. 1441–1444, Jan. 2021, doi: 10.1016/j.matpr.2020.08.122.

[35] “ss_microscope_roughness_equipment_img_1_01_1578247.jpg (783×300).” Accessed: Apr. 28, 2024. [Online]. Available: https://www.keyence.com/Images/ss_microscope_roughness_equipment_img_1_01_1578247.jpg

[36] P. H. Osanna and P. Totewa, “Workpiece accuracy — the critical path to economical production,” *Int. J. Mach. Tools Manuf.*, vol. 32, no. 1, pp. 45–49, Feb. 1992, doi: 10.1016/0890-6955(92)90059-P.

[37] M. Kurita, M. Sato, and K. Nakano, “A Technique for Rapidly Measuring Surface Roughness Using a Laser,” *JSME Int. J. Ser 1 Solid Mech. Strength Mater.*, vol. 35, no. 3, pp. 335–339, 1992, doi: 10.1299/jsmea1988.35.3_335.

[38] H. Wang, “Theoretical analysis and measurements on near specular scattering,” *Opt. Lasers Eng.*, vol. 27, no. 3, pp. 285–296, Jun. 1997, doi: 10.1016/S0143-8166(96)00024-3.

[39] “word-image-21.jpg (850×602).” Accessed: Apr. 28, 2024. [Online]. Available: https://www.tribonet.org/wp-content/uploads/2022/09/word-image-21.jpg

[40] “Surface Roughness | Measurements.” Accessed: Apr. 29, 2024. [Online]. Available: https://www.biolinscientific.com/measurements/surface-roughness

[41] “Surface roughness,” *Wikipedia*. Jan. 11, 2024. Accessed: Apr. 29, 2024. [Online]. Available:

https://en.wikipedia.org/w/index.php?title=Surface_roughness&oldid=1194911696#References

[42] B. Richter, T. Radel, and F. E. Pfefferkorn, “Sensitivity of surface roughness to laser parameters used for polishing additively manufactured Co-Cr alloy,” *Surf. Coat. Technol.*, vol. 451, p. 128872, Dec. 2022, doi: 10.1016/j.surfcoat.2022.128872.

[43] W. Jinlong, M. Yuxin, P. Wenjie, B. Yongjie, and S. Zeyu, “Evaluation of the effect of surface roughness parameters on fatigue of TC17 titanium alloy impeller using machine learning algorithm and finite element analysis,” *Eng. Fail. Anal.*, vol. 153, p. 107586, Nov. 2023, doi: 10.1016/j.engfailanal.2023.107586.

[44] J. Gockel, L. Sheridan, B. Koerper, and B. Whip, “The influence of additive manufacturing processing parameters on surface roughness and fatigue life,” *Int. J. Fatigue*, vol. 124, pp. 380–388, Jul. 2019, doi: 10.1016/j.ijfatigue.2019.03.025.

[45] M. Boujelbene, “Influence of the CO2 laser cutting process parameters on the Quadratic Mean Roughness *Rq* of the low carbon steel,” *Procedia Manuf.*, vol. 20, pp. 259–264, Jan. 2018, doi: 10.1016/j.promfg.2018.02.038.

[46] H. Itoga, K. Tokaji, M. Nakajima, and H.-N. Ko, “Effect of surface roughness on step-wise *S–N* characteristics in high strength steel,” *Int. J.*

Fatigue, vol. 25, no. 5, pp. 379–385, May 2003, doi: 10.1016/S0142-1123(02)00166-4.

[47] J. Wang, Y. Zhang, Q. Sun, S. Liu, B. Shi, and H. Lu, "Giga-fatigue life prediction of FV520B-I with surface roughness," *Mater. Des.*, vol. 89, pp. 1028–1034, Jan. 2016, doi: 10.1016/j.matdes.2015.10.104.

[48] X. Wu *et al.*, "Investigation on surface quality in micro milling of additive manufactured Ti6Al4V titanium alloy," *J. Manuf. Process.*, vol. 101, pp. 446–457, Sep. 2023, doi: 10.1016/j.jmapro.2023.05.110.

[49] A.-R. Alao, "Review of ductile machining and ductile-brittle transition characterization mechanisms in precision/ultraprecision turning, milling and grinding of brittle materials," *Precis. Eng.*, vol. 88, pp. 279–299, Jun. 2024, doi: 10.1016/j.precisioneng.2024.02.012.

[50] "Milling (machining)," *Wikipedia*. Apr. 18, 2024. Accessed: Apr. 30, 2024. [Online]. Available: https://en.wikipedia.org/w/index.php?title=Milling_(machining)&oldid=1219544953#References

[51] "How to use a Milling Machine - Instructions." Accessed: Apr. 30, 2024. [Online]. Available: https://www.americanmachinetools.com/how_to_use_a_milling_machine.htm

[52] “5-side-milling-300x232.png (300×232).” Accessed: Apr. 30, 2024. [Online]. Available: https://www.autodesk.com/products/fusion-360/blog/wp-content/uploads/2018/05/5-side-milling-300x232.png

[53] “Grinding (abrasive cutting),” *Wikipedia*. Mar. 20, 2024. Accessed: Apr. 30, 2024. [Online]. Available: https://en.wikipedia.org/w/index.php?title=Grinding_(abrasive_cutting)&oldid=1214732596

[54] B. Zhang, S. Wu, D. Wang, S. Yang, F. Jiang, and C. Li, “A review of surface quality control technology for robotic abrasive belt grinding of aero-engine blades,” *Measurement*, vol. 220, p. 113381, Oct. 2023, doi: 10.1016/j.measurement.2023.113381.

[55] H. Du, Y. Sun, D. Feng, and J. Xu, “Automatic robotic polishing on titanium alloy parts with compliant force/position control,” *Proc. Inst. Mech. Eng. Part B J. Eng. Manuf.*, vol. 229, no. 7, pp. 1180–1192, Jul. 2015, doi: 10.1177/0954405414567518.

[56] Q. Fan, Z. Gong, B. Tao, Y. Gao, Z. Yin, and H. Ding, “Base position optimization of mobile manipulators for machining large complex components,” *Robot. Comput.-Integr. Manuf.*, vol. 70, p. 102138, Aug. 2021, doi: 10.1016/j.rcim.2021.102138.

[57] J. W. Park, H. U. Cho, C. W. Chung, Y. S. Lee, and D. J. Jeon, “Modeling and grinding large sculptured surface by robotic digitization,” *J. Mech. Sci. Technol.*, vol. 26, no. 7, pp. 2087–2091, Jul. 2012, doi: 10.1007/s12206-012-0520-6.

[58] “Figure 1. Simplified diagram of the grinding process, adapted from [2].,” ResearchGate. Accessed: Apr. 30, 2024. [Online]. Available: https://www.researchgate.net/figure/Simplified-diagram-of-the-grinding-process-adapted-from-2_fig1_328511522

[59] “Polishing (metalworking),” *Wikipedia*. Apr. 25, 2024. Accessed: Apr. 30, 2024. [Online]. Available: https://en.wikipedia.org/w/index.php?title=Polishing_(metalworking)&oldid=1220736300

[60] “Fig.1. Schematic of single-axes polishing methods,” ResearchGate. Accessed: Apr. 30, 2024. [Online]. Available: https://www.researchgate.net/figure/Schematic-of-single-axes-polishing-methods_fig1_325609688

[61] “Sandblasting,” *Wikipedia*. Apr. 01, 2024. Accessed: Apr. 30, 2024. [Online]. Available: https://en.wikipedia.org/w/index.php?title=Sandblasting&oldid=1216681126

[62] I. Miturska-Barańska, A. Rudawska, and E. Doluk, “The Influence of Sandblasting Process Parameters of Aerospace Aluminium Alloy Sheets on Adhesive Joints Strength,” *Materials*, vol. 14, no. 21, Art. no. 21, Jan. 2021, doi: 10.3390/ma14216626.

[63] “Fatigue testing,” *Wikipedia*. Apr. 03, 2024. Accessed: Apr. 30, 2024. [Online]. Available: https://en.wikipedia.org/w/index.php?title=Fatigue_testing&oldid=1217052299

[64] P. Edwards and M. Ramulu, “Fatigue performance evaluation of selective laser melted Ti–6Al–4V,” *Mater. Sci. Eng. A*, vol. 598, pp. 327–337, Mar. 2014, doi: 10.1016/j.msea.2014.01.041.

[65] B. Baufeld, E. Brandl, and O. van der Biest, “Wire based additive layer manufacturing: Comparison of microstructure and mechanical properties of Ti–6Al–4V components fabricated by laser-beam deposition and shaped metal deposition,” *J. Mater. Process. Technol.*, vol. 211, no. 6, pp. 1146–1158, Jun. 2011, doi: 10.1016/j.jmatprotec.2011.01.018.

[66] E. Brandl, B. Baufeld, C. Leyens, and R. Gault, “Additive manufactured Ti-6Al-4V using welding wire: comparison of laser and arc beam deposition and evaluation with respect to aerospace material specifications,” *Phys. Procedia*, vol. 5, pp. 595–606, Jan. 2010, doi: 10.1016/j.phpro.2010.08.087.

[67] S. Leuders *et al.*, “On the mechanical behaviour of titanium alloy TiAl6V4 manufactured by selective laser melting: Fatigue resistance and crack growth performance,” *Int. J. Fatigue*, vol. 48, pp. 300–307, Mar. 2013, doi: 10.1016/j.ijfatigue.2012.11.011.

[68] C. Qiu, N. J. E. Adkins, and M. M. Attallah, “Microstructure and tensile properties of selectively laser-melted and of HIPed laser-melted Ti–6Al–4V,” *Mater. Sci. Eng. A*, vol. 578, pp. 230–239, Aug. 2013, doi: 10.1016/j.msea.2013.04.099.

[69] “compass.” Accessed: Apr. 30, 2024. [Online]. Available: https://compass.astm.org/document/?contentCode=ASTM%7CE0606-04%7Cen-US&proxycl=https%3A%2F%2Fsecure.astm.org&fromLogin=true

[70] “Figure 3. Fatigue test experimental setup.,” ResearchGate. Accessed: Apr. 30, 2024. [Online]. Available: https://www.researchgate.net/figure/Fatigue-test-experimental-setup_fig6_291808635

[71] A. Menghini *et al.*, “Fatigue analysis of hybrid steel construction parts using LPBF on hot-rolled steel,” *J. Constr. Steel Res.*, vol. 215, p. 108513, Apr. 2024, doi: 10.1016/j.jcsr.2024.108513.

[72] A. Yadollahi and N. Shamsaei, “Additive manufacturing of fatigue resistant materials: Challenges and opportunities,” *Int. J. Fatigue*, vol. 98, pp. 14–31, May 2017, doi: 10.1016/j.ijfatigue.2017.01.001.

[73] W. W. Wits and E. Amsterdam, “Fatigue prediction and life assessment method for metal laser powder bed fusion parts,” *CIRP Ann.*, vol. 72, no. 1, pp. 129–132, Jan. 2023, doi: 10.1016/j.cirp.2023.03.011.

[74] M. Bemani, S. Parareda, D. Casellas, A. Mateo, R. Das, and A. Molotnikov, “Rapid fatigue evaluation of additive manufactured specimens: Application to stainless steel AISI 316L obtained by laser metal powder bed fusion,” *Int. J. Fatigue*, vol. 184, p. 108279, Jul. 2024, doi: 10.1016/j.ijfatigue.2024.108279.

[75] D. Goetz, J. Diller, K. Achatz, and M. F. Zaeh, “Shrink line impact on the fatigue resistance of Inconel 718 parts manufactured by powder bed fusion of metals using a laser beam,” *J. Manuf. Process.*, vol. 115, pp. 481–490, Apr. 2024, doi: 10.1016/j.jmapro.2024.02.030.

[76] S. Wu and P. Dong, “Modeling of distributed defects and a proposed fatigue interaction criterion for additively manufactured metal parts,” *Int. J. Press. Vessels Pip.*, vol. 206, p. 105048, Dec. 2023, doi: 10.1016/j.ijpvp.2023.105048.

[77] P. Foti, N. Razavi, A. Fatemi, and F. Berto, “Multiaxial fatigue of additively manufactured metallic components: A review of the failure mechanisms and fatigue life prediction methodologies,” *Prog. Mater. Sci.*, vol. 137, p. 101126, Aug. 2023, doi: 10.1016/j.pmatsci.2023.101126.

[78] M. Wang *et al.*, “Tailored microstructure by using in-situ re-scanning and its influence on fatigue crack growth behavior of Inconel 718 fabricated by LPBF

at elevated temperature," *Int. J. Fatigue*, vol. 176, p. 107865, Nov. 2023, doi: 10.1016/j.ijfatigue.2023.107865.

[79] M. J. Markham and A. Fatemi, "Multiaxial fatigue life predictions of additively manufactured metals using a hybrid of linear elastic fracture mechanics and a critical plane approach," *Int. J. Fatigue*, vol. 178, p. 107979, Jan. 2024, doi: 10.1016/j.ijfatigue.2023.107979.

[80] R. Verma, S. Gairola, P. Kumar, and R. Jayaganthan, "Fracture toughness and fatigue crack growth behaviour of laser powder bed fusion (LPBF) built Ti-6Al-4V alloy through XFEM," *Procedia Struct. Integr.*, vol. 46, pp. 175–181, Jan. 2023, doi: 10.1016/j.prostr.2023.06.030.

[81] E. Maleki *et al.*, "Fatigue performance of U-notched additively manufactured AlSi10Mg parts: The effects of chemical and thermal post-treatments," *Addit. Manuf. Lett.*, vol. 7, p. 100175, Dec. 2023, doi: 10.1016/j.addlet.2023.100175.

[82] "compass." Accessed: Apr. 30, 2024. [Online]. Available: https://compass.astm.org/document/?contentCode=ASTM%7CD7774-17%7Cen-US&proxycl=https%3A%2F%2Fsecure.astm.org&fromLogin=true

[83] "Figure 2 Flexural Fatigue Test (after NCHRP 9-44[21])," ResearchGate. Accessed: Apr. 30, 2024. [Online]. Available:

https://www.researchgate.net/figure/Flexural-Fatigue-Test-after-NCHRP-9-4421_fig2_327568585

[84] D. Ordnung, J. Metelkova, A. Cutolo, and B. Van Hooreweder, “Improving fatigue performance of metal parts with up-facing inclined surfaces produced by laser powder bed fusion and in-situ laser remelting,” *Addit. Manuf. Lett.*, vol. 3, p. 100049, Dec. 2022, doi: 10.1016/j.addlet.2022.100049.

[85] S. Zaland *et al.*, “Experimental study on the flexural fatigue performance of geopolymeric recycled aggregate concrete,” *Constr. Build. Mater.*, vol. 418, p. 135451, Mar. 2024, doi: 10.1016/j.conbuildmat.2024.135451.

[86] Q. Xu and X. Wang, “Experimental study on high-cycle flexural fatigue behavior of cement mortar for ballastless track of high-speed railway,” *Constr. Build. Mater.*, vol. 385, p. 131525, Jul. 2023, doi: 10.1016/j.conbuildmat.2023.131525.

[87] A. Li, Z. Yang, S. Liu, Y. Liu, and H. Liu, “Experimental study on flexural fatigue behavior of composite T-beams in ultra-high performance concrete reinforced and normal-strength concrete,” *Int. J. Fatigue*, vol. 167, p. 107330, Feb. 2023, doi: 10.1016/j.ijfatigue.2022.107330.

[88] K. M. Hijazi, H. Mao, D. W. Holdsworth, S. J. Dixon, and A. S. Rizkalla, “Cyclic flexural fatigue of porous Ti6Al4V constructs for use in mandibular

reconstruction," *Int. J. Fatigue*, vol. 185, p. 108329, Aug. 2024, doi: 10.1016/j.ijfatigue.2024.108329.

[89] X. Tian, Z. Fang, S. Liu, Y. Xiang, Q. Zhu, and Y. Shao, "Flexural fatigue behavior of ultra-high performance concrete under low temperatures," *Cem. Concr. Compos.*, vol. 150, p. 105550, Jul. 2024, doi: 10.1016/j.cemconcomp.2024.105550.

[90] M. Carroll and M. Lisin, "Examination of Fracture Surfaces," Jan. 2024, doi: 10.31399/asm.hb.v12.a0006845.

[91] N. W. Sachs, "Understanding the surface features of fatigue fractures: How they describe the failure cause and the failure history," *J. Fail. Anal. Prev.*, vol. 5, no. 2, pp. 11–15, Apr. 2005, doi: 10.1361/15477020522924.

[92] A. Pineau, A. A. Benzerga, and T. Pardoen, "Failure of metals I: Brittle and ductile fracture," *Acta Mater.*, vol. 107, pp. 424–483, Apr. 2016, doi: 10.1016/j.actamat.2015.12.034.

[93] J. F. Knott, *Fundamentals of Fracture Mechanics*. Gruppo Italiano Frattura, 1973.

[94] J. Besson, D. Moinereau, and D. Steglich, *Local Approach to Fracture*. Presses des MINES, 2006.

[95] D. François, A. Pineau, and A. Zaoui, *Mechanical Behaviour of Materials: Volume II: Fracture Mechanics and Damage*. Springer Science & Business Media, 2012.

[96] F. M. Beremin, A. Pineau, F. Mudry, J.-C. Devaux, Y. D'Escatha, and P. Ledermann, "A local criterion for cleavage fracture of a nuclear pressure vessel steel," *Metall. Trans. A*, vol. 14, no. 11, pp. 2277–2287, Nov. 1983, doi: 10.1007/BF02663302.

[97] A. Pineau and T. Pardoen, "2.06 - Failure of Metals," in *Comprehensive Structural Integrity*, I. Milne, R. O. Ritchie, and B. Karihaloo, Eds., Oxford: Pergamon, 2007, pp. 684–797. doi: 10.1016/B0-08-043749-4/02109-1.

[98] "Fig. 10. SEM micrograph of ductile fracture surface of specimen 7.," ResearchGate. Accessed: Apr. 30, 2024. [Online]. Available: https://www.researchgate.net/figure/SEM-micrograph-of-ductile-fracture-surface-of-specimen-7_fig2_271879766

[99] "Figure 33: SEM image of fracture surface showing brittle fracture...," ResearchGate. Accessed: Apr. 30, 2024. [Online]. Available: https://www.researchgate.net/figure/SEM-image-of-fracture-surface-showing-brittle-fracture-behavior-and-secondary-cracks-on_fig21_360095526

[100] “compass.” Accessed: Apr. 30, 2024. [Online]. Available: https://compass.astm.org/document/?contentCode=ASTM%7CB0215-20%7Cen-US&proxycl=https%3A%2F%2Fsecure.astm.org&fromLogin=true

[101] “compass.” Accessed: Apr. 30, 2024. [Online]. Available: https://compass.astm.org/document/?contentCode=ASTM%7CB0822-20%7Cen-US&proxycl=https%3A%2F%2Fsecure.astm.org&fromLogin=true

Vita

Cristian Banuelos earned his Bachelor of Science in Mechanical Engineering in May 2022 from The University of Texas at El Paso, where he honed his engineering skills and developed a passion for advanced additive manufacturing techniques. Throughout his academic journey, Cristian had the privilege of working as a Research Assistant at the W.M. Keck Center, affiliated with the University of Texas at El Paso, where he contributed to cutting-edge research in 3D printing materials and processes. Additionally, he worked as a TA and Assistant Instructor for the Department of Aerospace and Mechanical Engineering where he had the chance to share his knowledge of CAD with the next generations undergraduate engineering students.

Contact Information: cbanuelos4@miners.utep.edu